UNIVERSIDADE DE LISBOA

FACULDADE DE CIÊNCIAS

DEPARTAMENTO DE FÍSICA

A Kinetic Framework for Particle–Environment Interactions in Active Matter

Ana Carolina Ricardo Ribeiro

Mestrado em Física e Astrofísica

Dissertação orientada por:

Nuno Araújo

Cristóvão Dias

2025

Acknowledgements

I would first like to thank my supervisors. To Nuno, whose brilliant pedagogical approach has shaped the way I think about physics. His insistence on focusing on the science itself—the "why" behind every step—has been invaluable, continuously pushing me to become a better and more thoughtful scientist. To Cristóvão, for the immense technical support, guidance, and patience he offered throughout this work. His help was essential, and I am deeply grateful for it.

My time at CFTC has been defined by the privilege of being surrounded by people driven by a genuine curiosity about physics and the world. Discussions were never limited to work-related problems: they often expanded into spontaneous questions, challenges scribbled on the board, and the joy of collectively trying to understand something new. I am deeply grateful for this environment—the companionship, the readiness to help, and the lively group meetings filled with valuable discussions. Beyond the science, I was fortunate to be part of a community that cared deeply about our shared working conditions and about improving the environment for students and researchers. The collective awareness, open conversations about what could be changed, and the sense of responsibility toward our community helped shape my understanding of what it means to contribute to a fair and supportive environment for people working together—something I will carry with me into any future workplace. I am also grateful to CFTC for supporting my participation in conferences, which made it possible to share and discuss this work with the wider scientific community.

To Henrique, for welcoming me from the very beginning and for teaching me how to navigate the social dynamics of the faculty. To Júlio, for the fun moments and uplifting presence. To Neves, for encouraging me to maintain a healthy balance between research and the many enriching aspects of life. To Vasco, for the many conversations that opened my eyes to the broader context of science. To Rafael, whose extraordinary breadth of knowledge made every discussion a pleasure. And to Daniel, for sharing my love of science communication and helping me appreciate the joy of hands-on, practical experimentation. Together we built a model of one of my favourite systems, the double pendulum, now hanging on the wall of CFTC.

I also want to thank my friends—especially Diogo, Lourenço, Lucas, and Duarte—for their companionship throughout this journey.

Finally, I want to express my deep appreciation to Fátima Mamad, who conducted the experiments presented here during her summer internship at CFTC, under my and Daniel Matias's supervision.
Thank you to everyone who shaped this work and the person I became throughout this process.

Resumo

Em física estatística, a matéria ativa, como células, micro-organismos ou micro-nadadores artificiais, constitui um exemplo paradigmático para o estudo de sistemas fora do equilíbrio, pois combina a não linearidade das interações com a quebra explícita da simetria temporal. Estes sistemas desafiam descrições termodinâmicas convencionais e permitem explorar novas classes de universalidade e mecanismos de auto-organização. Estas partículas convertem energia localmente para gerar movimento autónomo, permitindo-lhes explorar o espaço, interagir entre si e responder de forma dinâmica ao meio envolvente. Como resultado, exibem uma ampla variedade de comportamentos coletivos — desde a formação espontânea de aglomerados e vórtices até à emergência de fluxos coletivos e padrões espaciais complexos. Estes fenómenos resultam de uma combinação de interações locais, flutuações estocásticas e restrições geométricas impostas pelo ambiente.

Em contextos naturais, as partículas ativas raramente se movem num espaço vazio: tipicamente encontram-se imersas em meios densos, heterogéneos ou deformáveis, compostos por outros agentes, obstáculos ou geometrias confinantes. Nestas condições, as interações entre partículas e meio deixam de ser unidirecionais; sempre que deslocam obstáculos, abrem caminhos ou alteram propriedades locais do meio, introduzem uma forma de memória ambiental, na qual o estado atual do sistema depende da sua história dinâmica. Este acoplamento entre partículas e ambiente é uma das chaves para compreender a auto-organização em sistemas fora do equilíbrio.

Esta tese investiga como a memória ambiental influencia a mobilidade, a organização espacial e a emergência de estruturas coletivas em sistemas de matéria ativa. O objetivo central é compreender de que forma a interação dinâmica entre partículas ativas e obstáculos móveis pode gerar comportamentos emergentes, mesmo na ausência de comunicação direta entre os constituintes. Partindo de estudos recentes sobre a mediação ambiental em matéria ativa, desenvolveu-se um estudo sistemático que combina teoria, simulação e uma comparação experimental macroscópica. O núcleo teórico assenta num modelo baseado em rede e no método de Monte Carlo Cinético (KMC), no qual partículas ativas se movem sobre uma rede discreta e interagem com partículas passivas móveis sujeitas a exclusão de volume. Cada partícula ativa possui uma orientação preferencial e executa processos de propulsão, difusão translacional e reorientação estocástica; as partículas passivas difundem e podem ser deslocadas, permitindo ao meio reorganizar-se sob ação das ativas. Para descrever explicitamente a interação com o meio, o modelo inclui dois mecanismos microscópicos: empurrão (deslocação local de cadeias curtas de obstáculos) e realinhamento induzido pelo meio. Estes mecanismos controlam, respetivamente, a transferência de momento

e a capacidade de escapar a bloqueios locais, estabelecendo uma retroação entre a persistência direcional e a reorganização ambiental.

A abordagem discreta adotada diferencia-se de formulações contínuas por permitir um controlo direto sobre os processos microscópicos de propulsão, colisão e realinhamento, mantendo uma interpretação cinética clara e um custo computacional reduzido. Este formalismo possibilita a análise sistemática de como mecanismos locais se traduzem em comportamentos coletivos emergentes, algo difícil de capturar em equações hidrodinâmicas contínuas.

Um primeiro passo foi a validação do modelo num sistema exclusivamente ativo. Na ausência de obstáculos móveis, o modelo reproduz de forma robusta as características da separação de fase induzida por motilidade (MIPS): à medida que a atividade aumenta, observa-se a passagem de um estado homogéneo para um regime bimodal de densidades locais, com coexistência de regiões densas e diluídas mesmo sem interações atrativas. Essa caracterização foi complementada por uma análise quantitativa baseada no deslocamento quadrático médio (MSD), confirmando o comportamento típico de uma partícula ativa livre e validando a consistência dinâmica do modelo.

Para estabelecer uma correspondência quantitativa entre a formulação discreta e descrições contínuas, derivou-se um mapeamento explícito entre as taxas microscópicas de KMC e os parâmetros efetivos. No caso unidimensional, obteve-se analiticamente o coeficiente de difusão efetivo de uma partícula ativa, o que fornece uma regra de correspondência direta entre parâmetros do modelo e grandezas contínuas. A introdução de um fator geométrico de mapeamento permite estender essa relação para diferentes geometrias, garantindo a interpretação coerente de regimes.

A formulação proposta oferece, portanto, uma estrutura versátil e extensível para o estudo de sistemas ativos e mistos, possibilitando a comparação direta com modelos contínuos e a investigação de fenómenos coletivos emergentes em meios confinados ou heterogéneos.

No estudo de misturas ativo–passivas com difusividades translacionais iguais, analisou-se como os mecanismos microscópicos modulam o transporte em meios densos. As simulações mostram que a difusão efetiva das partículas ativas cresce monotonicamente com a probabilidade de realinhamento, refletindo a facilitação de descongestionamento por rotação. Em contraste, a dependência com a probabilidade de empurrar é não monotónica: valores intermédios maximizam a mobilidade ao converter bloqueios locais em deslocamentos cooperativos. As curvas de deslocamento quadrático médio exibem o cruzamento balístico–difusivo típico de movimento ativo, mas com uma região intermédia marcada por canais transitórios, indicativos de uma memória ambiental.

A tese prossegue com o estudo de misturas ativo-passivas com difusividades translacionais diferentes. Mostra-se que aumentar a mobilidade passiva atua como parâmetro de controlo que suprime a formação de domínios densos e restaura a mistura homogénea. A partir das flutuações do maior aglomerado passivo, realizou-se uma análise de tamanho finito para testar a existência de criticalidade. Embora a transição se acentue sistematicamente com o tamanho do sistema, os expoentes efetivos revelaram-se não universais, dependendo fortemente do torque de realinhamento. Esta sensibilidade a parâmetros microscópicos, em vez de uma mudança de classe de universalidade, demonstra o carácter específico de cada sistema em transições de fase fora do equilíbrio. A falha do colapso de dados completo corrobora a interpretação de que se trata de um crossover não crítico, embora sistemático, evidenciando a natureza distintamente fora

do equilíbrio da separação de fases em misturas ativo-passivas.

Por fim, desenvolveu-se uma comparação macroscópica com robôs da escala do centímetro, usados como análogos de partículas ativas em arenas com obstáculos móveis de geometria cúbica e cilíndrica. Foi construída uma arena com fronteiras curvas, concebidas para mitigar a acumulação junto às paredes. Observa-se que obstáculos cúbicos promovem estruturas rígidas e bloqueios locais, enquanto cilindros favorecem trajetórias mais fluídas e reorganizações dinâmicas. Medições da velocidade efetiva dos obstáculos revelam uma dependência acentuada com a massa, decaindo mais rapidamente do que o previsto por colisões inelásticas, o que confirma o papel dominante de dissipação e do contacto intermitente. A comparação com as simulações mostra uma correspondência qualitativa entre aumento de massa experimental e redução da eficiência de empurrão no modelo, validando o quadro mecanístico proposto.

Em conjunto, os resultados demonstram que a inclusão explícita do acoplamento dinâmico entre partículas e meio é essencial para descrever a transição entre regimes de congestão, mistura e separação de fases em matéria ativa. O modelo proposto fornece uma ponte entre descrições microscópicas e contínuas, e constitui uma base para estender o estudo a outro tipo de meios e interações. Estas ideias abrem caminho para uma compreensão mais profunda da auto-organização em sistemas biológicos e robóticos ativos.

Palavras Chave: Matéria ativa, ambientes complexos, separação de fases, sistemas fora do equilíbrio, Monte Carlo Cinético.

Abstract

Active particles, such as cells, microorganisms, or microrobots are paradigmatic examples of collective dynamics far from equilibrium. They locally convert energy to generate self-propulsion, leading to complex behaviors including clustering, vortex formation, and emergent flows. In realistic environments, active particles interact with complex or deformable media, leading to a rich variety of collective behaviors that emerge from feedback between particle motion and medium dynamics.

This thesis investigates how such feedback influences mobility, spatial organization, and the emergence of collective structures in active–passive mixtures. A discrete kinetic model based on the Kinetic Monte Carlo method was developed, in which active particles self-propel, diffuse, and interact with mobile passive obstacles through excluded volume and medium-induced realignment. Two microscopic mechanisms — pushing and realignment — govern momentum transfer and the ability to escape local jamming.

In the purely active limit, the model reproduces motility-induced phase separation. A mean-squared displacement analysis confirms the expected ballistic–diffusive crossover and validates the dynamic consistency of the formulation. An explicit mapping between microscopic KMC rates and hydrodynamic parameters establishes quantitative links to continuum theories.

In dense mixtures with uniform diffusivity across species, the interplay between pushing and realignment controls transport: rotation facilitates unjamming, while intermediate pushing strengths maximize mobility. For mixtures with a diffusivity contrast between species, increasing passive mobility suppresses clustering and restores homogeneous mixing. Finite-size scaling shows the transition sharpens systematically with system size, but the associated effective exponents are non-universal and depend on the torque, indicating a sensitivity of the demixing process to microscopic interaction rules rather than a shift of universality class. A macroscopic experiment using centimeter-scale robots in arenas with mobile obstacles qualitatively reproduces the simulated trends, confirming the mechanistic interpretation.

The framework establishes a quantitative bridge between discrete kinetic models and continuum active-matter descriptions, providing insight into how microscopic interactions govern emergent transport and phase behavior.

Keywords: Active matter, complex environments, phase separation, non-equilibrium systems, Kinetic Monte Carlo.

Contents

List of Figures

Chapter 1

Introduction

Carpenter ants are expert navigators, not just because they follow pheromone trails, but because they physically reshape their environment. By moving twigs, leaves, and other debris, they build bridges and tunnels [1] that facilitate collective motion. This behavior exemplifies *stigmergy*, a form of indirect communication in which individuals modify a shared environment, leaving behind cues that guide future actions. Although stigmergy was first studied in social insects, it emerges more broadly in systems where structure and motion co-evolve, from bacterial colonies tracing nutrient gradients [2] to artificial microswimmers and robotic swarms [3] whose trajectories are influenced by environmental cues [4].

The emergence of complex, collective behavior from many simple interacting units is observed across physics, chemistry, biology, and social science [5, 6, 7, 8, 9]. A primary goal, particularly in physics, is to capture such emergent phenomena using a minimal set of principles. This approach has succeeded in equilibrium thermodynamics, providing unifying laws that apply from the electronic properties of materials to the motion of planets. For systems far from equilibrium, however, this remains a central challenge. A particularly important class is active matter: collections of units that consume energy to generate directed motion [10]. Because they continually dissipate energy, these systems are intrinsically out of equilibrium and exhibit behaviors not possible in equilibrium settings, including flocking [6], clustering [11], vortex formation [12], and spontaneous self-organization [10].

Active matter is deeply rooted in biological systems, where motility arises from energy-consuming self-propulsion mechanisms. Many microorganisms, including bacteria, spermatozoa, and unicellular algae, move by converting chemical energy into directed motion [13, 14]. At larger scales, collective motility underpins crucial physiological processes such as tissue growth, wound healing and cancer metastasis [15].

In recent years, advances in micro- and nanoscale fabrication have made it possible to engineer artificial self-propelled particles that mimic these biological behaviors [12, 16, 17, 18, 19, 20, 21, 22]. These synthetic “microswimmers” serve as controllable model systems for exploring the physical principles of active motion: they can reproduce key features of living motility while enabling systematic tests of how propulsion, noise, and interactions give rise to collective dynamics. In this sense, biological and artificial

active matter jointly provide the experimental foundation for understanding nonequilibrium organization.

To understand how microscopic interactions give rise to such dynamics, one needs coarse-grained models that reduce microscopic detail while retaining the mechanisms of emergence. A key question is how much of this complex organization can be captured by physical models based on a minimal set of rules. Put differently, how much physics is needed to achieve a degree of complexity that resembles biological motion phenomena. It is important to stress that the aim of such models is not to mimic any specific organism in detail, but to provide a general framework for analyzing far-from-equilibrium systems.

Building on this principle, this thesis develops a minimal lattice-based Kinetic Monte Carlo (KMC) model of active particles coupled to a dynamic environment. The model captures how particles shape their surroundings and, in turn, have their dynamics modulated by the structures they generate and encounter. The aim is to identify the essential ingredients that enable environment-mediated organization in active matter.

This thesis is organized as follows. Chapter 2 introduces the modeling framework. It begins with the Active Brownian Particle formalism and summarizes previous studies in crowded environments, before presenting the Kinetic Monte Carlo approach developed here. The model formulation, numerical implementation, and mapping between continuum and lattice descriptions are described in detail, followed by validation through translational and rotational dynamics and by reproducing Motility Induced Phase Separation. Chapter 3 investigates active–passive mixtures with uniform diffusivity, focusing on how self-propulsion influences passive clustering, structure formation, and transport when both species share the same translational diffusion coefficient. Chapter 4 extends this framework to active–passive mixtures with diffusivity contrast, using finite-size scaling to test for criticality in the demixing transition and exploring how the associated scaling trends depend on microscopic interaction rules. Chapter 5 presents a tabletop experiment that illustrates environment-mediated organization in a macroscopic setting, providing qualitative analogies with the model predictions. Finally, the appendices compile supporting material: Appendix A provides a decision flowchart for model implementation; Appendices B and C describe parameter mappings between continuum and lattice quantities; and Appendix D details the derivation of time increments in the KMC algorithm.

Chapter 2

Model and Methods

Several theoretical and computational models [23] have been developed to describe the behavior of active particles, ranging from microscopic particle-based simulations [24, 25, 26, 27, 28, 29, 30, 31] that include explicit interparticle potentials to continuum approaches based on effective fields [11, 32, 33, 34, 35]. These models differ in their level of detail, computational complexity, and the physical phenomena they capture, and are typically chosen to suit the spatial and temporal scales or particular scientific questions of interest.

2.1 Active Brownian Particle (ABP) Framework

The Active Brownian Particle (ABP) model offers a minimal yet powerful description that captures the essential features of self-propelled motion. In this approach, particles move at constant speed with their orientation undergoing rotational diffusion, effectively modeling the stochastic reorientation due to interactions with the surrounding fluid and thermal fluctuations. The influence of the fluid medium and other microscopic forces is incorporated implicitly through an effective Langevin force, balancing persistent active propulsion with stochastic noise. At the microscopic scale typical of the systems we consider, such as bacteria or synthetic microswimmers, the inertial effects are negligible because of the low Reynolds number and the dominance of viscous damping. For this reason, the dynamics of active Brownian particles are well captured by an overdamped description, where frictional forces and stochastic fluctuations set the properties of motion.

Although the specific model developed in this thesis does not employ the particle-based equations of active Brownian dynamics directly, it is instructive to introduce them here. They provide a minimal theoretical framework that highlights the essential contributions of propulsion, diffusion, and noise in active systems, and serve as a useful reference point for contrasting the lattice-based approach developed later. In the overdamped regime, the particle's position $\mathbf{r}(t) = (x(t), y(t))$ evolves according to [10, 17, 36]:

$$\begin{aligned}\dot{x}(t) &= \sqrt{2D_T}\,\eta_x(t) + v_0\cos(\theta(t)),\\ \dot{y}(t) &= \sqrt{2D_T}\,\eta_y(t) + v_0\sin(\theta(t)),\\ \dot{\theta}(t) &= \sqrt{2D_R}\,\eta_\theta(t),\end{aligned} \tag{2.1}$$

where v_0 is the propulsion speed, $\theta(t)$ the propulsion orientation, and D_T and D_R the translational and rotational diffusion coefficients, respectively. The stochastic terms $\eta_x(t)$, $\eta_y(t)$, and $\eta_\theta(t)$ are independent Gaussian white-noise processes with zero mean and unit variance, i.e.,

$$\langle \eta_i(t)\rangle = 0, \qquad \langle \eta_i(t)\,\eta_j(t')\rangle = \delta_{ij}\,\delta(t-t'), \quad i,j \in \{x,y,\theta\}, \tag{2.2}$$

representing thermal and environmental fluctuations.

A central quantity used to characterize stochastic trajectories is the Mean Square Displacement (MSD),

$$\langle \Delta r^2(t)\rangle = \left\langle |\mathbf{r}(t) - \mathbf{r}(0)|^2 \right\rangle,$$

which measures how far a particle typically wanders after a given time t. For ABPs in two dimensions, the exact MSD [17] is

$$\langle \Delta r^2(t)\rangle = \left[4D_T + 2v_0^2\tau_R\right]t + 2v_0^2\tau_R^2\left(e^{-t/\tau_R} - 1\right), \tag{2.3}$$

where the characteristic persistence time is

$$\tau_R = \frac{1}{D_R}. \tag{2.4}$$

Derivations and detailed comparisons to passive Brownian motion can be found in [37]. This expression interpolates between two distinct transport regimes. For short times $t \ll \tau_R$, the propulsion orientation has not yet randomized, and the trajectory is approximately straight (ballistic). In this regime, the MSD grows as

$$\langle \Delta r^2(t)\rangle \sim v_0^2 t^2. \tag{2.5}$$

For long times $t \gg \tau_R$, successive reorientations wash out directional persistence, and the motion crosses over to diffusive behavior. The MSD then grows linearly in time with an effective diffusion coefficient

$$D_{\text{eff}} = D_T + \tfrac{1}{2}v_0^2\tau_R, \tag{2.6}$$

which exceeds passive thermal diffusion, reflecting activity-enhanced transport.

Two characteristic scales naturally emerge from this analysis. The persistence time τ_R sets the timescale over which directed motion is maintained before reorientations dominate, while the corresponding persistence length,

$$l_R = v_0\tau_R, \tag{2.7}$$

defines the spatial extent of this directed "run". Together, l_R and τ_R provide the fundamental dynamical scales of an active particle, separating short-time ballistic motion from long-time diffusion. These scales are particularly useful for comparing experiments and models, since they collapse the rich stochastic dynamics of an ABP into two physically meaningful parameters.

Thus, the ABP framework captures the essential single-particle physics of active matter. However, real environments often include interactions, obstacles, and multi-particle effects. Important physical mechanisms such as hydrodynamic interactions, shape anisotropy, and crowding are neglected here but become critical in dense or confined regimes. These complexities motivate the use of extended models, which consider other possible interactions.

2.2 Previous Studies in Crowded Environments

Active agents rarely move through empty space; in natural and artificial systems alike, they are often surrounded by other agents or passive obstacles—from cells migrating through tissue and molecular motors operating inside the cytoplasm to robots and pedestrians navigating crowded spaces [38, 35, 39]. Such environments, particularly when composed of both active and passive components, fundamentally alter individual motion and collective dynamics. Crowding and confinement, rather than acting as neutral backgrounds, can enhance correlations and promote emergent organization across scales [40, 41].

The transport of living and synthetic active species through crowded environments plays a crucial role in many natural and engineered processes [42, 43]. In these settings, the effective transport properties of motile microorganisms depend on the interplay between swimmer motility and the boundaries that define the porous environment [44, 42]. Even passive Brownian particles experience significant slowdowns in dense or obstructed media: steric hindrance, hydrophobic and electrostatic interactions, and purely excluded-volume effects can substantially hinder diffusive flux, even at low obstacle concentrations [45, 46, 47]. For active particles, local slowdowns within boundary layers can strongly influence their overall mobility across porous or heterogeneous materials [42]. Soft, deformable environments such as mucus, hydrogels, or polymeric networks add further complexity, since surface fluctuations and elastic deformations feed back into particle motion and can drastically reshape effective transport pathways [42]. Together, these effects highlight how environmental structure fundamentally shapes transport at both the single-particle and collective level.

Crowding and confinement therefore act as powerful catalysts for self-organization: the spontaneous emergence of large-scale structure from local interactions without central control. Through repeated microscopic interactions under environmental constraints, collective patterns arise with properties and functions absent at the level of single particles, often spanning scales much larger than the constituents themselves. It is now widely recognised that confinement and crowding do not merely restrict motion, but also reshape effective interactions, impose symmetry breaking, and modify encounter dynamics in ways that steer organization [48].

Understanding how active particles behave in such environments is crucial for uncovering the fun-

damental mechanisms that underlie structure formation, collective motion, and self-organization across biological, soft matter, and engineered systems. Building on these ideas, several experimental studies have explored how environmental structure mediates coordination and transport.

One illustrative case is the formation and reuse of transient paths, a form of coordination rooted in stigmergy—indirect communication through environmental modification. Dias et al. demonstrated this principle in colloidal swimmers navigating disordered landscapes, where swimmers followed transient trails left by their predecessors [4]. Counterintuitively, crowding enhanced coordination: path reuse was mediated by a torque that mechanically aligned swimmers along the trail boundaries, creating a shared environmental memory that even a single particle could later exploit for more efficient search [49]. This finding illustrates how, in decentralized systems of active units lacking explicit signaling pathways, the environment itself can mediate coordination.

In a different system, Makarchuk et al. showed that forward scattering of motile bacteria around micro-obstacles strengthens their propagation along surfaces, as cells maintain directional persistence while avoiding large deflections [50]. Together, these studies illustrate a general principle: the environment is not passive but can act as an active mediator of coordination and collective transport. Similar mechanisms are thought to operate in biological collectives, where environmental shaping enables feedback between motion and structure.

Motivated by these findings, the present work employs a lattice-based Kinetic Monte Carlo (KMC) framework to investigate active particles moving through dynamic environments of passive obstacles. We explore how obstacle interactions, environmental crowding, and feedback mechanisms give rise to path reuse, clustering, and emergent collective motion.

2.3 Model

Computer simulations are invaluable for exploring the parameter space of active matter systems and for revealing emergent phenomena that are often impractical or inaccessible in experiment. By systematically varying interaction rules and conditions, simulations provide theoretical insight into the rules governing collective behavior.

A variety of computational approaches exist for modeling active matter, each optimized for particular spatial and temporal scales. Molecular Dynamics (MD) simulations, for example, can accurately resolve the trajectories of individual particles, capturing the effects of particle shape and detailed interaction forces when these are relevant [51]. However, for systems with many particles or when fine solvent details are not critical, MD becomes computationally expensive and impractical for studying large-scale collective dynamics. To access longer timescales and larger system sizes, coarse-grained or mesoscale methods — such as Langevin dynamics (which incorporate stochastic and frictional terms to model omitted degrees of freedom) or dissipative particle dynamics (DPD) — trade spatial detail for computational efficiency, making them more suitable for exploring emergent collective phenomena [52, 53, 23]. In the next section, we discuss how such mesoscale frameworks can be applied in the context of active matter.

For the present study, the focus is on emergent collective dynamics, where the essential features are governed by effective interaction rules rather than atomistic detail. In this regime, the Kinetic Monte Carlo (KMC) method is particularly well-suited. Unlike standard Metropolis Monte Carlo, KMC is a rejection-free algorithm that incorporates physical time by directly advancing the system through successive state-to-state transitions. This enables efficient simulation of long timescales and large system sizes without tracking every microscopic motion [54].

2.3.1 Kinetic Monte Carlo (KMC) Framework

The Kinetic Monte Carlo (KMC) method models the stochastic evolution of a system by treating its dynamics as a sequence of discrete uncorrelated events occurring randomly in time. Instead of resolving all microscopic fluctuations, the method advances the system between well-defined states, with each possible transition associated with a characteristic rate. Events are selected according to their relative probabilities, making KMC a rejection-free alternative to standard Monte Carlo: every step produces a physically meaningful transition. Importantly, KMC explicitly advances time by assigning exponentially distributed waiting periods to events, thereby reproducing the correct temporal evolution.

A standard lattice-based KMC simulation follows a well-defined sequence of steps. First, the system is initialized, for example with particles placed on lattice sites in a chosen configuration. For each state, all possible dynamical events—such as particle movements, rotations, or reactions—are enumerated. Each event type i is characterized by a rate constant W_i, and if n_i realizations are available (allowed events will depend on interaction rules and constraints), its total contribution is

$$R_i = n_i W_i. \tag{2.8}$$

Summing over all types yields the overall rate

$$R_{\text{tot}} = \sum_i R_i. \tag{2.9}$$

An event type j is then chosen with probability R_j/R_{tot}, using a uniform random number $\eta \in [0, R_{\text{tot}})$. From the n_j possible realizations of this event type, one is selected uniformly at random, and the system configuration is updated accordingly. The elapsed physical time before the event occurs is drawn from the exponential distribution,

$$\Delta t = -\frac{\ln(u)}{R_{\text{tot}}}, \tag{2.10}$$

where $u \in (0, 1)$ is another uniform random number (see Appendix D for derivation). This form arises because the sequence of events in KMC constitutes a Poisson process: events occur independently with total rate R_{tot}, so the waiting time between successive events is exponentially distributed. This cycle of event identification, selection, execution, and time advancement is repeated until a stopping criterion is met, such as reaching a maximum simulation time or steady state.

In this work, space is represented by a discrete lattice. This approximation balances physical interpretability with computational efficiency: while lattice discretization omits microscopic details below the lattice spacing, the observables of interest, such as clustering, transport, or path formation, emerge at scales much larger than the lattice unit. By encoding motion and interaction rules at the lattice level [55], one can systematically explore the impact of minimal ingredients on emergent dynamics.

Like any modeling framework, KMC requires choices regarding which processes are explicitly represented as stochastic events. This modularity is a strength: additional processes can be incorporated iteratively if results suggest they play a significant role. Prior studies have demonstrated that KMC accurately captures both kinetic pathways and statistical properties [56, 57] across a wide range of systems [54, 58, 59, 60, 61], making it a versatile and powerful tool for investigating self-organization and transport in active matter.

2.3.2 Numerical Implementation

Building on the lattice KMC framework introduced above, our model is implemented on a discrete two-dimensional square lattice of size $N = L \times L$. The lattice representation sacrifices space resolution but retains essential physical ingredients, such as excluded volume interactions and directional propulsion, while remaining computationally efficient. This allows the simulation of large systems over long timescales, both of which are critical for probing emergent collective behavior.

Particles are hard-core and occupy a single lattice site. Both active and passive particles have identical size, but differ in their dynamics. The initial configuration is generated by randomly placing a density of $\rho_a = \frac{N_a}{L^2}$ active and $\rho_p = \frac{N_p}{L^2}$ passive particles uniformly on the lattice without overlap. Active particles possess a discrete orientation corresponding to one of the four lattice axes, reflecting the underlying square symmetry. Each particle is initially assigned a random orientation that defines its propulsion direction. This discretization introduces anisotropy into single-particle trajectories, an effect that will be revisited in Section 2.3.3. Passive particles, in contrast, have no orientation and do not self-propel.

For computational efficiency, lattice sites are encoded by integer values: 0 for an empty site; 1–4 for an active particle oriented left (1), down (2), right (3), or up (4); and 5 for a passive particle.

Without considering interactions, each active particle undergoes three types of events, illustrated in Fig. 2.1:

1. **Active propulsion:** hopping one site forward at rate ϵ,
2. **Thermal diffusion:** hopping one site forward at rate ξ,
3. **Rotational diffusion:** changing orientation by $\pm 90°$ at rate ω.

Passive particles undergo only thermal diffusion. Here, ϵ controls the strength of active propulsion, ξ sets the thermal hopping rate, and ω governs rotational noise. Together, propulsion and reorientation sustain persistent random walks with a mean persistence time $\tau_p \sim \omega^{-1}$. The rate ξ effectively sets the

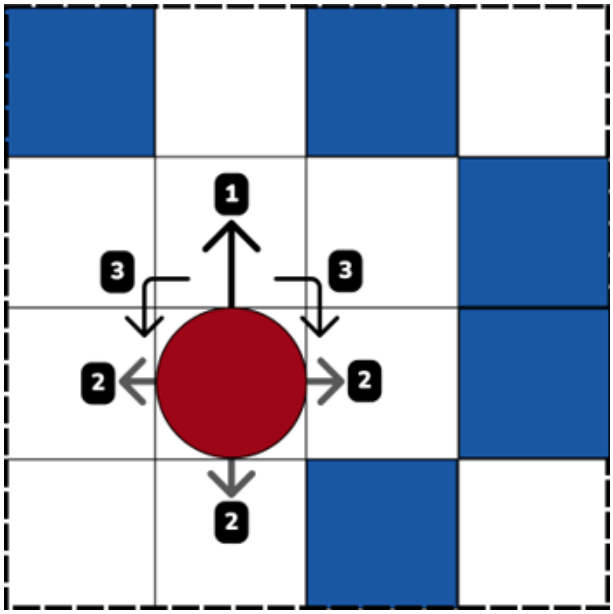

Figure 2.1: Underlying rules for particle dynamics. Active particles (red) can move in their preferential direction (1), diffuse thermally into other directions (2), or rotate (3). Passive particles (blue) perform only thermal diffusion (2). A lattice of size $N = L \times L$ is shown with periodic boundary conditions. Shapes are schematic; all particles occupy a single lattice site.

translational temperature of the system. In Chapter 3, a single value of ξ is used for both active and passive particles; a generalized model allowing distinct translational temperatures for the two species will be introduced in Chapter 4.

So far, the dynamics describe isolated particles. We now incorporate interactions between active particles and their environment, consisting of both other active particles and passive obstacles. These interactions are implemented through excluded-volume rules that give rise to two additional processes: pushing and realigning. When an active particle attempts to move into an occupied site during propulsion (Process 1), one of the following outcomes occurs (Fig. 2.2):

a) **Push:** if the number of consecutively occupied sites in the propulsion direction is less than or equal to a model parameter m, the active particle pushes the entire chain one lattice site forward. Rate π.

b) **Realignment:** if pushing is not performed, the particle may instead change its orientation by $\pm 90°$, allowing it to attempt movement into a free neighboring site. Rate Ω.

c) **Bounce-back:** if neither a) nor b) lead to a free site, the particle remains at its current position.

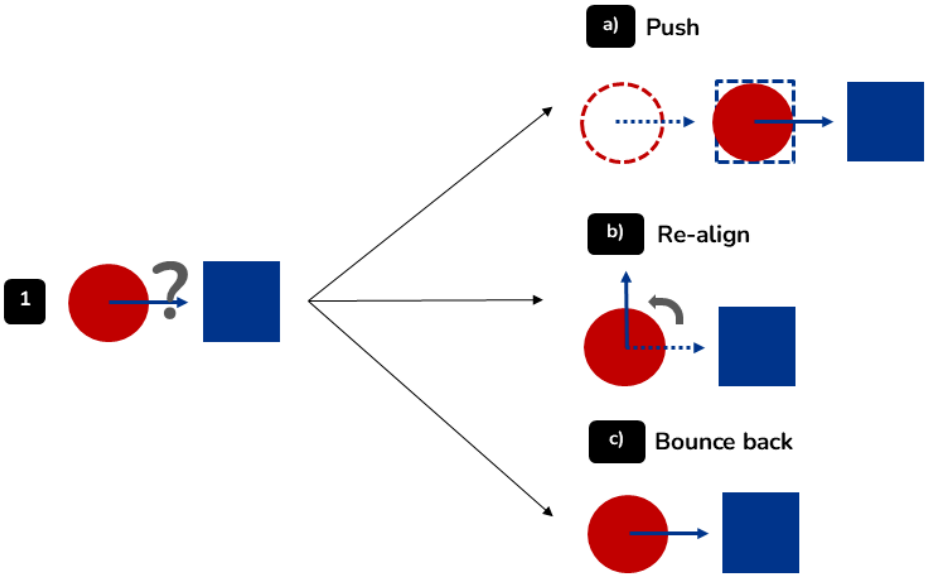

Figure 2.2: Interaction processes for active particles encountering obstacles: a) pushing up to m obstacles (rate π), b) realigning to $\pm 90°$ (rate Ω), or c) bouncing back if neither process succeeds. Active particles are shown in red, passive ones in blue; arrows indicate propulsion direction.

The relative probabilities of pushing a) and realigning b) are tuned by the parameters π, Ω, and m, where π and Ω control the respective rates of pushing and realigning, while m determines the maximum length of a consecutive chain of obstacles that an active particle can push. The algorithm is designed to be rejection-free in the traditional Kinetic Monte Carlo sense; at every iteration, a process is always selected and executed from the list of all possible events. The bounce-back outcome c) is not represented by an explicit kinetic rate; rather, it is the deterministic consequence of an attempted move that cannot be realized by either pushing or realigning. In this case, the particle's position and orientation remain unchanged while the simulation clock is advanced. This avoids artificially introducing a high-frequency "failed move" event while still capturing the physical effect of a collision blockade.

A complete flowchart of the active-particle decision rules is provided in Appendix A. Periodic boundary conditions are applied in both lattice directions to minimize edge effects and mimic an effectively infinite system. The lattice side length L is selected sufficiently large to ensure that emergent phenomena develop at length scales well above the lattice discretization.

Time evolution proceeds through event-driven KMC steps as described in Section 2.3.1. At each step, the algorithm evaluates all potential microscopic events for each particle and calculates the total system rate as the sum of rates of all currently allowed events. An event is considered "allowed" only if it does not violate model constraints such as excluded volume or the pushing limit m.

Explicitly, the total rate at time t is given by:

$$R_{\text{tot}}(t) = N_{\text{active}}(t)\,\beta + N_{\text{diff}}(t)\,\xi + N_{\text{rot}}(t)\,\omega, \tag{2.11}$$

where $N_{\text{active}}(t)$ denotes the number of allowed active propulsion attempts at time t, i.e., particles whose target site is either empty or can be vacated by pushing a chain of length $\leq m$. $N_{\text{diff}}(t)$ counts allowed thermal diffusion hops into empty neighboring sites for both active and passive particles, while $N_{\text{rot}}(t) = 2N_a$ accounts for clockwise and counterclockwise rotations of all active particles. Rotational diffusion events are always allowed, as their feasibility does not depend on neighboring site occupancy.

2.3.3 Parameter Mapping (Continuum to Lattice)

To connect the parameters used in our lattice-based simulations to their continuum counterparts, it is necessary to systematically map each fundamental rate and coefficient. This enables robust comparison with theoretical predictions and allows physical interpretation of simulation data.

The first step is translating the rotational diffusion implemented in the lattice model into a rotational diffusion coefficient for continuous space. In our lattice model, rotational diffusion corresponds to a discrete two-dimensional random walk, where the particle's orientation changes in increments of $\pm\frac{\pi}{2}$ with equal probability at each step. These unbiased turning rates, denoted by ω, result in no net drift. A detailed derivation (Appendix C) shows that the rotational diffusion coefficient D_R in continuous space is related to the 2D lattice ($\Delta\theta = \frac{\pi}{2}$) rate ω by:

$$D_R = \omega \frac{\pi^2}{8}. \tag{2.12}$$

This mapping factor $\frac{\pi^2}{8}$ accounts for the discretization of rotational increments, enabling direct comparison between lattice simulation and continuum theory.

The corresponding persistence time, which quantifies how long a particle maintains its orientation before reorienting due to rotational diffusion, is then the inverse of D_R:

$$\tau_R = \frac{1}{D_R} = \frac{8}{\pi^2 \omega}. \tag{2.13}$$

With the rotational mapping established, we next relate the effective translational diffusion coefficient to its lattice analogs. The analytical expression (Eq. 2.3) for the MSD of an active particle in continuum theory assumes isotropic motion, whereas our simulations use discrete lattice geometries for computational feasibility. In the lattice, motion is restricted to a finite set of directions defined by its symmetry (e.g., $n = 4$ for a square lattice).

To account for deviations introduced by this discretization, we introduce a geometric mapping factor α, which modifies the active contribution to the effective diffusion coefficient (Eq. 2.6). Using the mapped persistence time τ_R (Eq. 2.13), the parameter mapping is given by:

$$D_{\text{eff}} = \xi + \frac{1}{2} \alpha \epsilon^2 \frac{8}{\pi^2 \omega}. \tag{2.14}$$

In this expression, the translational diffusion coefficient is given by the lattice parameter, $D_T = \xi$, and the effective self-propulsion speed corresponds directly to the activity rate, $v = \epsilon$. The geometric mapping factor α accounts for the effect of angular discretization on the lattice.

While our primary model uses a square lattice with angular discretization $n = 4$, to quantify how α depends on directional resolution, we performed auxiliary simulations with a single active particle (disabling push and torque interactions), varying the number of allowed orientation directions n. This isolates the influence of angular discretization on the mapping factor.

Figure 2.3 displays the results for the mapping factor $\alpha - 1$ as a function of n. The decay of $\alpha - 1$ is well described by a power law,

$$\alpha - 1 = \frac{A}{n^k} \tag{2.15}$$

with fitted parameters $A \approx 5.1 \pm 0.2$ and $k \approx 2.03 \pm 0.03$.

The mapping factor α decreases rapidly as n increases, reflecting the convergence of the discrete lattice model to the continuum limit with finer angular resolution.

Based on this general behavior, we then focus on the fixed $n = 4$ case corresponding to our lattice geometry. For this end, we take MSD curves for varying translational diffusion rate ξ, with fixed angular resolution $n = 4$, active propulsion strength $\epsilon = 2$, and rotational diffusion rate $\omega = 0.1$. The measured slopes in the diffusive regime allows us to extract the mapping factor $\alpha = 1.276 \pm 0.008$. Consequently, using all the mapping relations previously stated, the effective diffusion coefficient reads for $n = 4$:

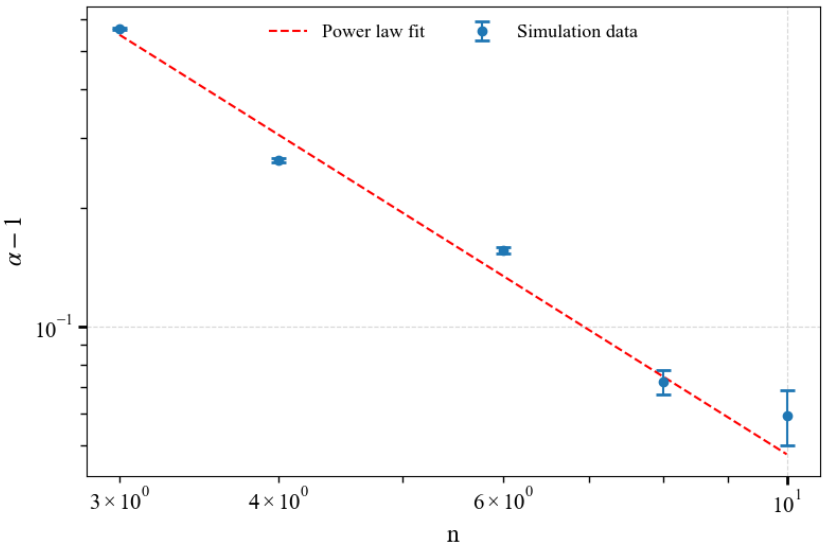

Figure 2.3: Log-log mapping factor $\alpha - 1$ as a function of angular discretization n. The red curve represents a power-law fit $\alpha - 1 = A/n^k$, with fitted parameters $A \approx 5.1 \pm 0.2$ and $k = 2.03 \pm 0.03$. Translational diffusion is fixed at $\xi = 0.0001$. Averaged over 10^4 samples.

$$D_{\text{eff}} = D_T + \frac{1}{2} 1.28 v^2 \tau_R. \tag{2.16}$$

For the 1D case, an analytical derivation of the effective diffusion coefficient is possible and is provided in Appendix B.

In 2D, the corresponding master equations can be written in analogy with the 1D case (Eqs. B.1). We consider a single active particle moving on a 2D discrete lattice, with spacings Δx and Δy along the x and y directions, respectively. The particle can move along its preferential direction with rate $\beta = \epsilon + \xi$, along transverse directions with rate ξ, and switch its orientation at rate ω. $P_{\rightarrow}(x, y, t)$, $P_{\leftarrow}(x, y, t)$, $P_{\uparrow}(x, y, t)$, and $P_{\downarrow}(x, y, t)$ denote the state probabilities of a particle occupying site (x, y) at time t with preferential orientation right, left, up, or down, respectively.

$$\begin{aligned}
\frac{\partial P_{\rightarrow}}{\partial t} &= \beta \left(P_{\rightarrow}(x - \Delta x, y, t) - P_{\rightarrow} \right) + \xi \left(P_{\leftarrow}(x, y - \Delta y, t) + P_{\leftarrow}(x, y + \Delta y, t) \right. \\
&\quad \left. + P_{\rightarrow}(x + \Delta x, y, t) - 3P_{\rightarrow} \right) + \omega \left(P_{\uparrow} + P_{\downarrow} - 2P_{\rightarrow} \right)
\end{aligned}$$

$$\begin{aligned}
\frac{\partial P_{\leftarrow}}{\partial t} &= \beta \left(P_{\leftarrow}(x + \Delta x, y, t) - P_{\leftarrow} \right) + \xi \left(P_{\leftarrow}(x, y - \Delta y, t) + P_{\leftarrow}(x, y + \Delta y, t) \right. \\
&\quad \left. + P_{\leftarrow}(x - \Delta x, y, t) - 3P_{\leftarrow} \right) + \omega \left(P_{\uparrow} + P_{\downarrow} - 2P_{\leftarrow} \right)
\end{aligned}$$

$$\begin{aligned}
\frac{\partial P_{\uparrow}}{\partial t} &= \beta \left(P_{\uparrow}(x, y - \Delta y, t) - P_{\uparrow} \right) + \xi \left(P_{\uparrow}(x + \Delta x, y, t) + P_{\uparrow}(x - \Delta x, y, t) \right. \\
&\quad \left. + P_{\uparrow}(x, y + \Delta y, t) - 3P_{\uparrow} \right) + \omega \left(P_{\leftarrow} + P_{\rightarrow} - 2P_{\uparrow} \right)
\end{aligned}$$

$$\begin{aligned}
\frac{\partial P_{\downarrow}}{\partial t} &= \beta \left(P_{\downarrow}(x, y + \Delta y, t) - P_{\downarrow} \right) + \xi \left(P_{\downarrow}(x + \Delta x, y, t) + P_{\downarrow}(x - \Delta x, y, t) \right. \\
&\quad \left. + P_{\downarrow}(x, y - \Delta y, t) - 3P_{\downarrow} \right) + \omega \left(P_{\leftarrow} + P_{\rightarrow} - 2P_{\downarrow} \right)
\end{aligned}$$

Performing a Taylor expansion in Δx and Δy up to second order yields the continuum-limit equations shown below. Specifically, we retain terms up to $\mathcal{O}(\Delta x^2, \Delta y^2)$ in the expansion of the discrete shifts, while higher-order terms are neglected. However, unlike in 1D, the resulting system of coupled partial differential equations for the four orientation-resolved probabilities does not admit a straightforward analytical treatment.

$$
\begin{aligned}
\frac{\partial P_{\rightarrow}}{\partial t} &= (\beta+\xi)\left(\frac{\Delta x^2}{2}\frac{\partial^2 P_{\rightarrow}}{\partial x^2}\right) + (\xi-\beta)\left(\Delta x\frac{\partial P_{\rightarrow}}{\partial x}\right) \\
&\quad + \xi\left(\Delta y^2\frac{\partial^2 P_{\rightarrow}}{\partial y^2}\right) + \kappa\left(P_{\uparrow}+P_{\downarrow}-2P_{\rightarrow}\right) \\
\frac{\partial P_{\leftarrow}}{\partial t} &= (\beta+\xi)\left(\frac{\Delta x^2}{2}\frac{\partial^2 P_{\leftarrow}}{\partial x^2}\right) + (\beta-\xi)\left(\Delta x\frac{\partial P_{\leftarrow}}{\partial x}\right) \\
&\quad + \xi\left(\Delta y^2\frac{\partial^2 P_{\leftarrow}}{\partial y^2}\right) + \kappa\left(P_{\uparrow}+P_{\downarrow}-2P_{\leftarrow}\right) \\
\frac{\partial P_{\uparrow}}{\partial t} &= (\beta+\xi)\left(\frac{\Delta y^2}{2}\frac{\partial^2 P_{\uparrow}}{\partial y^2}\right) + (\xi-\beta)\left(\Delta y\frac{\partial P_{\uparrow}}{\partial y}\right) \\
&\quad + \xi\left(\Delta x^2\frac{\partial^2 P_{\uparrow}}{\partial x^2}\right) + \kappa\left(P_{\leftarrow}+P_{\rightarrow}-2P_{\uparrow}\right) \\
\frac{\partial P_{\downarrow}}{\partial t} &= (\beta+\xi)\left(\frac{\Delta y^2}{2}\frac{\partial^2 P_{\downarrow}}{\partial y^2}\right) + (\beta-\xi)\left(\Delta y\frac{\partial P_{\downarrow}}{\partial y}\right) \\
&\quad + \xi\left(\Delta x^2\frac{\partial^2 P_{\downarrow}}{\partial x^2}\right) + \kappa\left(P_{\leftarrow}+P_{\rightarrow}-2P_{\downarrow}\right)
\end{aligned}
$$

For 2D, the continuum limit leads to a system of coupled PDEs for which no closed-form solution could be obtained. Several standard numerical schemes were evaluated, but none yielded results consistent with the effective diffusion measured in simulations.

For this reason, the Taylor expansion is retained only to document the formal continuum limit of the lattice model. The quantitative value of the 2D effective diffusion coefficient is therefore taken directly from simulation results rather than an analytical expression.

These mapping relationships are essential to accurately translate the rotational dynamics observed in lattice simulations into the continuous-space framework. This enables rigorous comparison with theoretical predictions and experimental observations. By establishing this connection, the current methodology lays a foundation for quantitatively bridging discrete simulation models with continuum descriptions of active matter.

2.3.4 Validation

Before analyzing interacting systems, it is essential to validate the simulation code against known theoretical results for a single ABP. Interaction parameters Ω, π and m are therefore equal to 0 throughout this section. This step verifies that both the translational and rotational dynamics are correctly implemented within our model's framework.

2.3.4.1 Translational dynamics

We simulated a single active Brownian particle ($N_a = 1$, $N_p = 0$) on a square lattice of size $L = 1000$ with periodic boundary conditions. The simulation parameters were chosen as active propulsion rate $\epsilon = 2$, rotational diffusion rate $\omega = 0.1$, and translational diffusion rate $\xi = 0.1$. Only the stochastic processes listed in Section 2.3.2 were included. The results were averaged over 10^4 independent trajectories to ensure statistical reliability.

Figure 2.4 shows the simulated MSD, validated against the theoretical ABP expression incorporating the correction factors derived in the previous chapter. Specifically, the effective diffusion coefficient D_{eff} used for comparison accounted for the geometric mapping factor α modifying the active contribution, while the rotational diffusion coefficient D_R was related to ω by the mapping formula from Section 2.3.3.

It should be noted that the factor α was derived for the effective diffusion coefficient, that is, in the diffusive regime corresponding to long times. For short times, however, this factor remains undetermined, which explains the slight deviation observed between the simulated curve and the analytical prediction. The agreement at long times confirms the accuracy of our numerical implementation of translational dynamics.

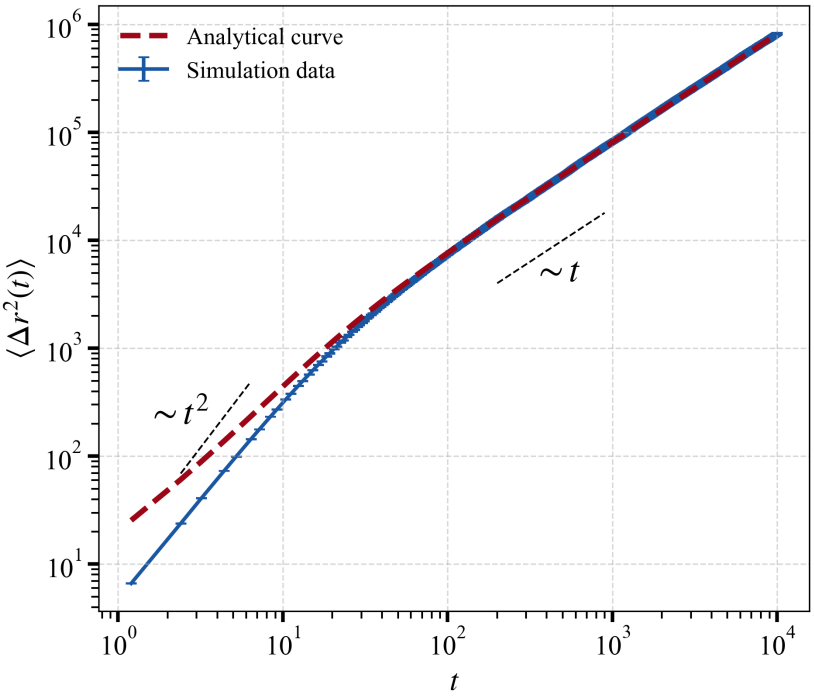

Figure 2.4: Mean-square displacement of a single active particle compared to the analytical prediction, including geometric and rotational diffusion mappings. Parameters: $\epsilon = 2$, $D_R = 0.123$, $D_T = 0.1$, $L = 1000$, averaged over 10^4 trajectories.

2.3.4.2 Rotational dynamics

Next, we validate the rotational dynamics of our model. In the continuous description, the propulsion orientation $\theta(t)$ undergoes pure rotational diffusion, modeled by the stochastic differential equation [36]

$$\dot{\theta}(t) = \sqrt{2D_R}\,\eta_\theta(t), \tag{2.17}$$

where $\eta_\theta(t)$ is Gaussian white noise. This implies that the angular MSD grows linearly with time:

$$\langle [\theta(t) - \theta(0)]^2 \rangle = 2D_R t. \tag{2.18}$$

In our lattice simulations, θ changes in discrete increments of $\pm\frac{\pi}{2}$ at a rate ω, which is mapped to the continuous rotational diffusion coefficient D_R as described in Section 2.3.3. To validate this, we measured the angular MSD for multiple values of ω and confirmed the expected linear growth with slope $2D_R$, demonstrating the validity of our rotational update rules (Fig. 2.5).

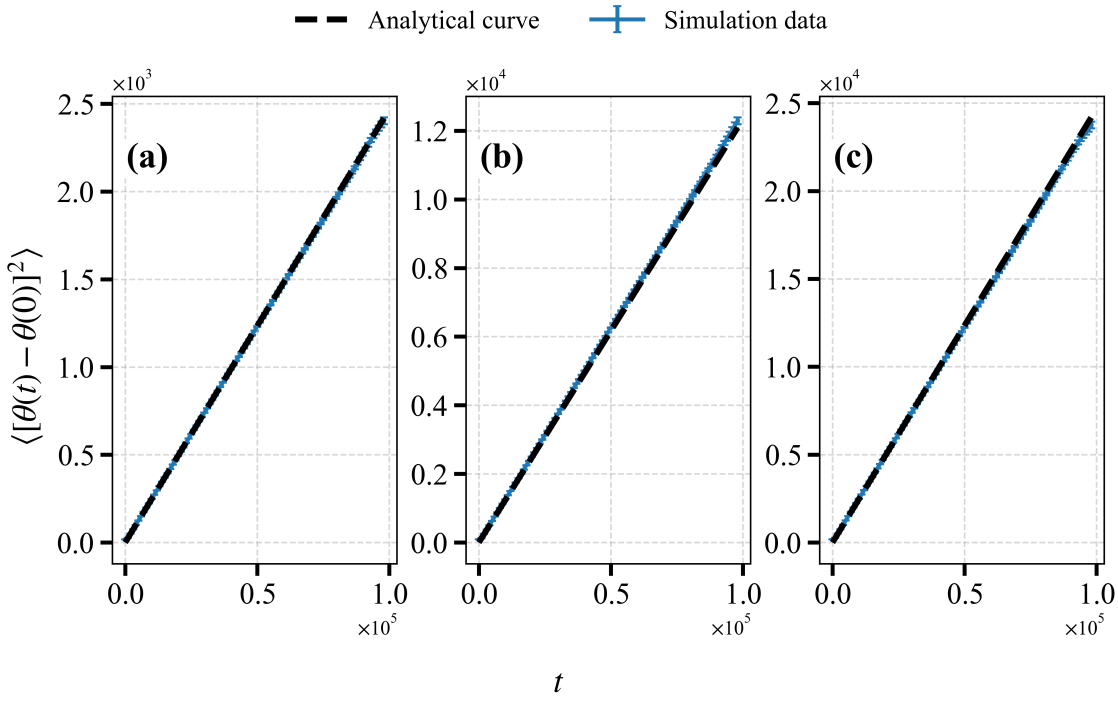

Figure 2.5: Angular mean-square displacement for different rotational diffusion coefficients: (a) $D_R = 0.012$, (b) $D_R = 0.062$, and (c) $D_R = 0.123$. Parameters: $\epsilon = 2$, $D_T = 0.001$, $L = 50$, averaged over 5 particles and 10^4 trajectories.

Additionally, we analyzed the distribution of orientations $P(\theta, t)$. By the central limit theorem, for

sufficiently long times this distribution converges to a Gaussian with variance $\sigma^2 = 2D_R t$:

$$P(\theta, t) = \frac{1}{\sqrt{4\pi D_R t}} \exp\left(-\frac{[\theta(t) - \theta(0)]^2}{4D_R t}\right). \tag{2.19}$$

Histograms of θ collected from many independent particles at fixed time collapse accurately onto the theoretical Gaussian distribution (Fig. 2.6), further supporting the correct implementation of rotational diffusion and mapping of ω to D_R.

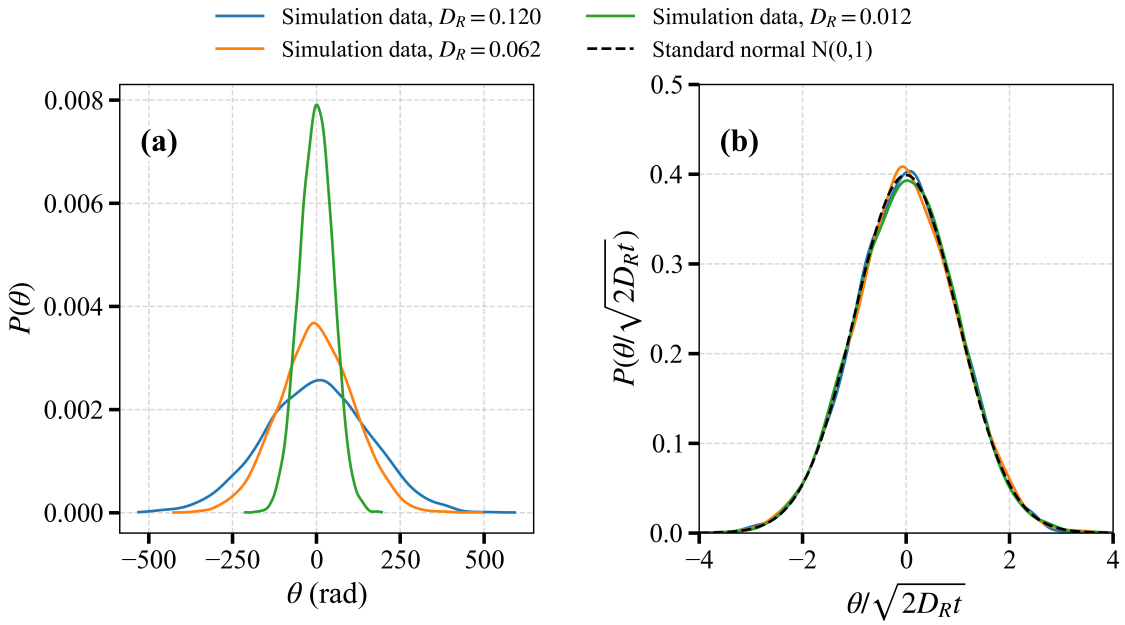

Figure 2.6: (a) Angular distribution $P(\theta, t)$ at $t = 10^5$ compared to the Gaussian with variance $2D_R t$. (b) Normalized distribution $P\left(\frac{\theta}{\sqrt{2D_R t}}\right)$ compared with the standard normal distribution $N(0, 1)$, confirming the expected rotational diffusion behavior. Parameters: $\epsilon = 2$, $D_T = 0.001$, $L = 50$, averaged over 5 particles and 10^2 trajectories.

Together, these benchmarks provide strong validation of our simulation code, confirming that the rotational dynamics reproduces the expected behavior of the active Brownian particle model in both MSD growth and orientation statistics.

2.3.4.3 Motility Induced Phase Separation (MIPS)

Motility Induced Phase Separation (MIPS) is a nonequilibrium phenomenon in which active particles with purely repulsive interactions spontaneously separate into coexisting dense and dilute phases — a behavior not achievable in passive equilibrium systems [11, 62, 63, 64]. This phase separation arises

because particles slow down in regions of high density, leading to accumulation and the formation of clusters [65, 66].

In the passive limit ($\epsilon = 0$), particles perform Brownian motion and distribute uniformly. Increasing activity ϵ alters this behavior through flux-driven dynamics: when particles become neighbors, their mobility is hindered. If the characteristic reorientation time is sufficiently long compared to the arrival time of other particles, clusters may grow. The competition between persistent self-propulsion and thermal and rotational diffusion governs the evolution towards either clustering or a homogeneous state [62, 66].

To validate that our model captures the essential physics of MIPS, we performed simulations varying particle activity ϵ and density ρ_a, analyzing cluster formation and phase coexistence. Simulations were performed on a 200×200 lattice with active particle density $\rho_a = 0.2$ and no passive particles ($\rho_p = 0$), using the rules defined in Figure 2.1.

Figure 2.7 illustrates snapshots of the system configuration at time $t = 10^4$ as activity ϵ increases. At low activity ($\epsilon = 2$), the system remains homogeneous. As ϵ increases, a dense cluster forms and grows, signaling the onset and development of MIPS. Color coding in the snapshots reflects particle orientations.

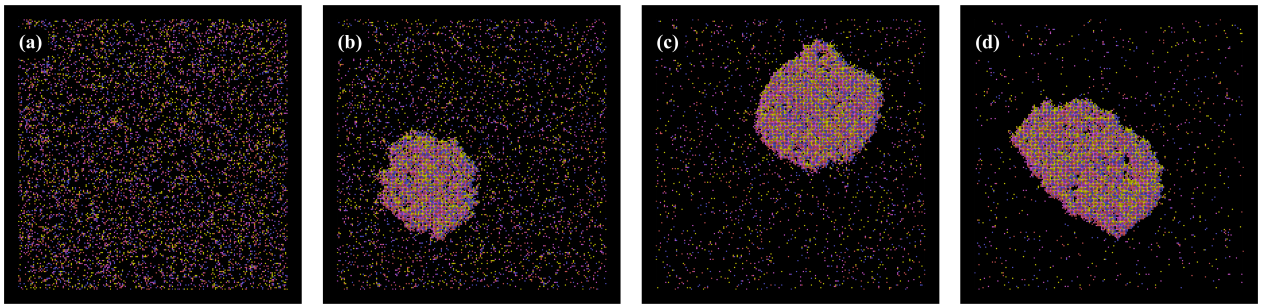

Figure 2.7: Snapshots at $t = 10^4$ for increasing activity ϵ with $\rho = 20\%$, $D_T = 1$, $D_R = 0.123$, and lattice size $L = 200$. (a) $\epsilon = 2$, (b) $\epsilon = 5$, (c) $\epsilon = 10$, (d) $\epsilon = 20$. The system evolves from a homogeneous state to one exhibiting macroscopic cluster formation as activity increases. Different colors indicate particle orientations.

To quantify clustering, the lattice was subdivided into 10×10 squares, and local densities were computed over 10^2 independent snapshots. Figure 2.8 shows the normalized density frequency histograms at final time $t = 10^4$. This coarse-graining method enables visualization of density fluctuations and identification of phase coexistence through bimodality.

At low activity ($\epsilon = 2$), the distribution is unimodal near the mean density $\rho_a = 0.2$, consistent with a homogeneous phase. Increasing ϵ induces a secondary peak at high density, indicating cluster nucleation. At higher activity, a clear bimodal distribution emerges, with peaks near zero and close to full occupancy, reflecting coexistence of dilute and dense phases—hallmarks of MIPS.

These results verify that our model robustly reproduces essential MIPS features, in quantitative agreement with continuum theories and prior experimental and computational studies on active matter. The

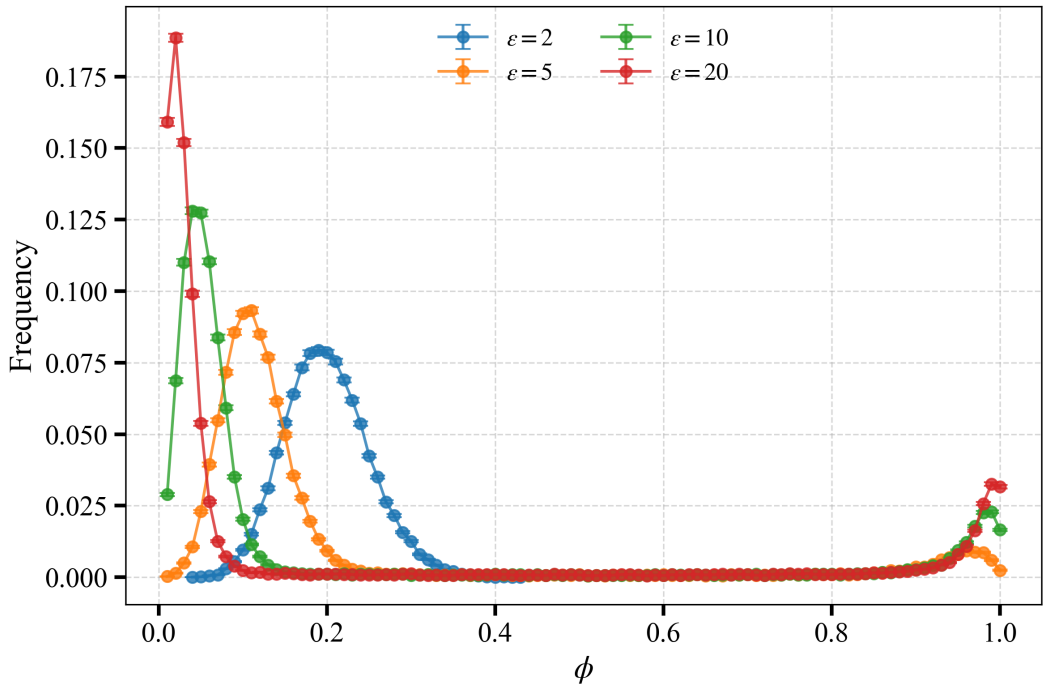

Figure 2.8: Density frequency distribution at $t = 10^4$ for varying activity ϵ. Parameters: $\rho_a = 0.2$, $D_T = 1$, $D_R = 0.123$, $L = 200$.

agreement between the simulated density distributions and the predicted bimodal coexistence confirms that the minimal lattice formulation retains the key ingredients of motility-induced phase separation.

Chapter 3

Active-Passive Mixtures with Uniform Diffusivity

This chapter introduces an extended model to study mixtures of active and passive particles. This lattice-based Kinetic Monte Carlo framework explicitly incorporates excluded-volume interactions between the two species, enabling investigation of how these couplings influence clustering, phase separation, and emergent collective phenomena.

Throughout this chapter, both active and passive particles share the same translational diffusion rate ξ, corresponding to equal effective temperatures. The effects of temperature mismatch between species will be addressed in Chapter 4. Here, we focus on two interrelated phenomena: (i) the spatial organization and clustering of passive particles, and (ii) the transport properties and dynamics of active particles in mixed environments.

3.1 Passive Clustering and Structure Formation

Passive clustering and structure formation are examined on a lattice of size $L = 200$ with particle densities $\rho_a = 1.1\%$ (active) and $\rho_p = 37.5\%$ (passive), and parameters $D_T = 0.0001$, $D_R = 0.123$, $\epsilon = 2$ and $m = 1$. Key parameters such as the push probability π and realignment probability Ω are systematically varied to characterize emergent passive spatial patterns and collective organization.

Pushing interactions in the model predominantly occur between active and passive particles due to the low density of active particles and the correspondingly small probability of active–active encounters. Consequently, the parameter π (push probability), together with the mass ratio m, effectively controls the relative inertia of the two species. Different values of π can thus be interpreted as tuning the relative influence of active propulsion on passive rearrangements, making this parameter an implicit proxy for the effective mass ratio. This subject is further discussed in Chapter 5.

Figure 3.1 shows representative snapshots of the system evolution under various parameter combinations. Initially, passive particles (blue) form transient, interconnected pathways and channels driven

by sparse active particles (red). These dynamic structures and their partial reuse over time indicate environment-mediated organization induced by active motion, reminiscent of previous observations in molecular dynamics studies [4].

At longer times, however, the system undergoes a robust transition beyond transient networks toward macroscopic phase separation. Following rapid initial rearrangements and cluster nucleation, the passive-particle move rate decays to a steady-state plateau (Fig. 3.3), indicating coexistence of stable dense passive-rich and dilute active-rich regions.

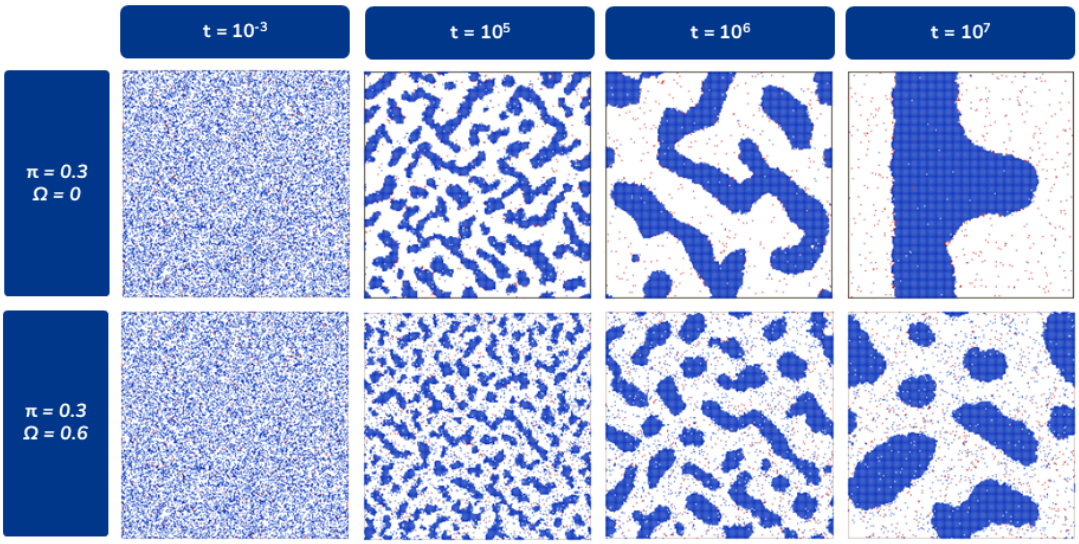

Figure 3.1: Snapshots of the time evolution, in KMC time units, of an active (red)-passive (blue) particle mixture at densities $\rho_p = 37.5\%$, $\rho_a = 1.1\%$ and activity $\epsilon = 2$. Push probability π and realignment probability Ω are varied across simulations.

As in Section 2.3.4.3, the lattice was subdivided into 10×10 squares, and local density measurements were aggregated over 10^2 independent snapshots to obtain coarse-grained density histograms, quantifying spatial heterogeneity in the passive-particle distribution.

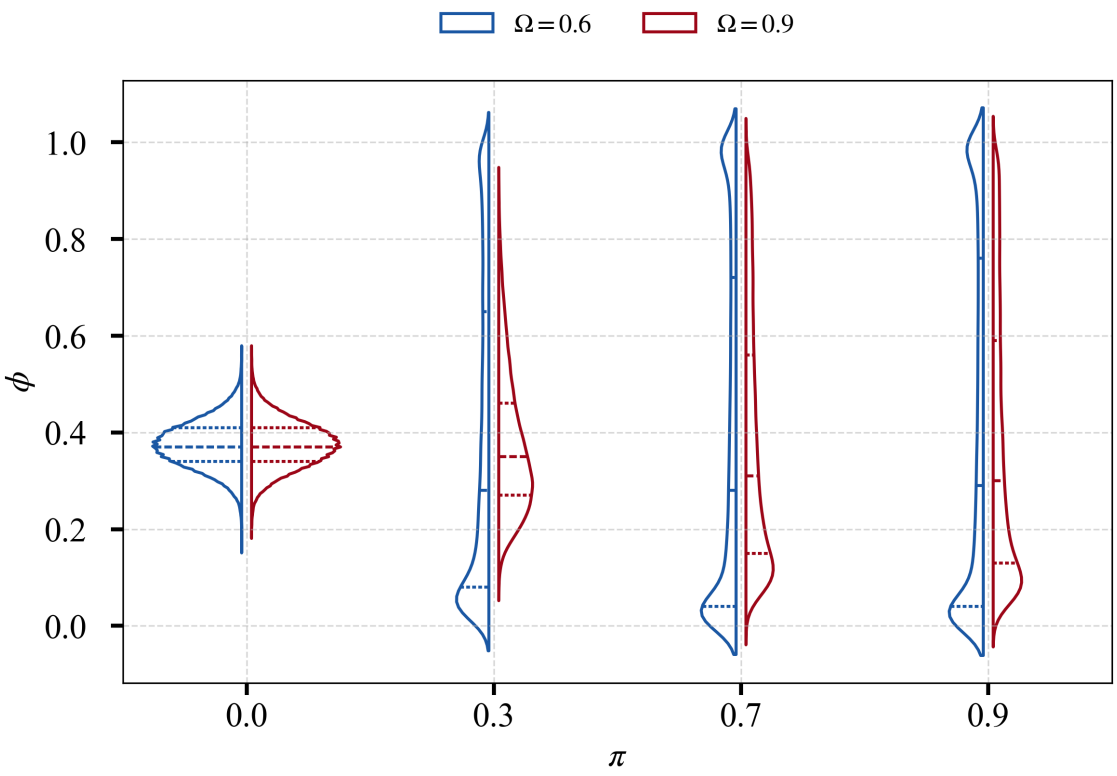

Figure 3.2: Local passive particle density distributions and corresponding snapshots at time $t = 10^6$. For $\pi = 0$, the distribution centers near $\rho_p = 37.5\%$, consistent with a uniform state. Increasing π at intermediate Ω leads to bimodal distributions with peaks near zero and one, indicative of phase separation into dilute and dense phases.

At zero push probability ($\pi = 0$), the system remains spatially uniform, with local densities centered around the global mean $\rho_p = 37.5\%$. As π increases (for intermediate Ω), the density histograms develop clear bimodality with peaks near zero and unity, signaling coexistence of dilute and dense domains. The onset of bimodality marks a nonequilibrium transition akin to motility-induced phase separation but mediated here by active–passive coupling.

Together, the density histograms and passive-particle move rate demonstrate that the system relaxes into a nonequilibrium steady state with stable phase-separated structures.

These findings highlight a key distinction from prior active–passive models: while short- and intermediate-time dynamics are dominated by transient channel formation reminiscent of earlier studies, the system ultimately evolves toward macroscopic phase separation rather than a sustained dynamic network. This behavior underscores how even sparse active components can drive large-scale organization in a predominantly passive matrix through mechanical feedback and local rearrangements.

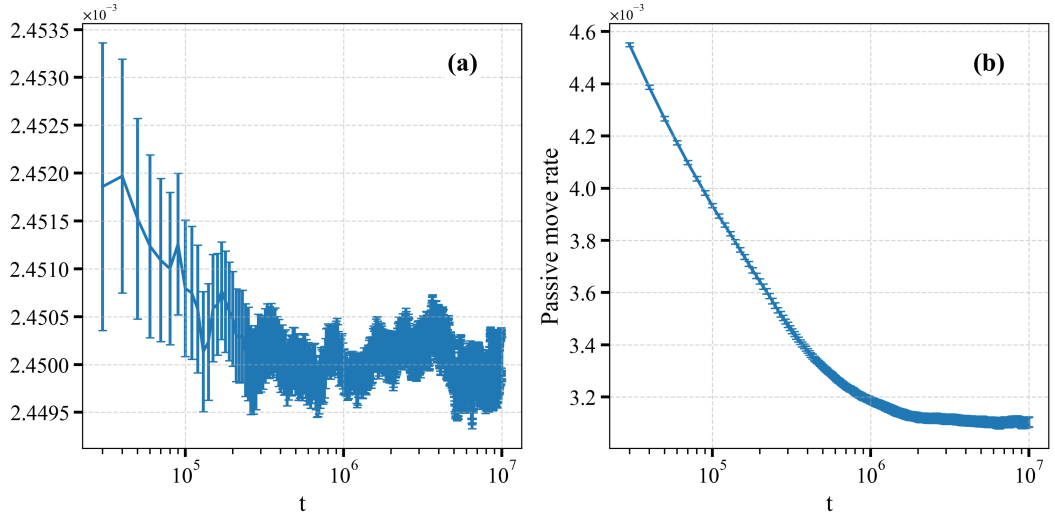

Figure 3.3: Passive particle move rate as a function of time for (a) $\pi = 0$ and (b) $\pi = 0.5$. The late-time plateau confirms the attainment of a stationary state. Averaged over 10^2 independent samples.

3.2 Active Transport and Dynamics

Understanding the transport properties of active particles within crowded, heterogeneous environments is crucial to characterizing their emergent collective behavior. In this section, we analyze the mean-square displacement (MSD) and effective diffusion of active particles embedded in passive particle matrices.

Simulations were performed in a lattice of size $L = 50$ with densities $\rho_p = 37.5\%$ and $\rho_a = 1.1\%$, and parameters $D_R = 0.123$, $\epsilon = 2$, $\pi = 0.5$ and $m = 1$. Each curve was averaged over 10^4 independent realizations.

The MSD curves in Figure 3.4 display the characteristic dynamical regimes of active Brownian motion. At short times, particles exhibit a ballistic increase, $\langle \Delta r^2(t) \rangle \sim t^2$, reflecting persistent propulsion before orientation decorrelation. This regime gradually transitions into an intermediate sub-ballistic behavior due to frequent encounters with passive obstacles and local confinement effects. At long times, the MSD converges toward a diffusive scaling, $\langle \Delta r^2(t) \rangle \sim 2D_{\text{eff}}t$, consistent with the analytical prediction for active Brownian particles (black dashed line).

Increasing the torque Ω reduced the rotational persistence time, promoting an earlier crossover to diffusion. This effect is evident from the earlier saturation of the MSD slope for higher Ω, particularly at small translational diffusivity $D_T = 0.0001$, where persistence dominates the short-time dynamics. In contrast, for larger $D_T = 0.001$, translational noise competes with active propulsion, yielding a smoother and earlier transition to diffusive scaling. The insets emphasize this crossover regime, confirming that at sufficiently long times the dynamics recover normal diffusion.

Figure 3.5 quantifies these trends through the effective diffusion coefficient D_{eff} for $D_T = 0.0001$.

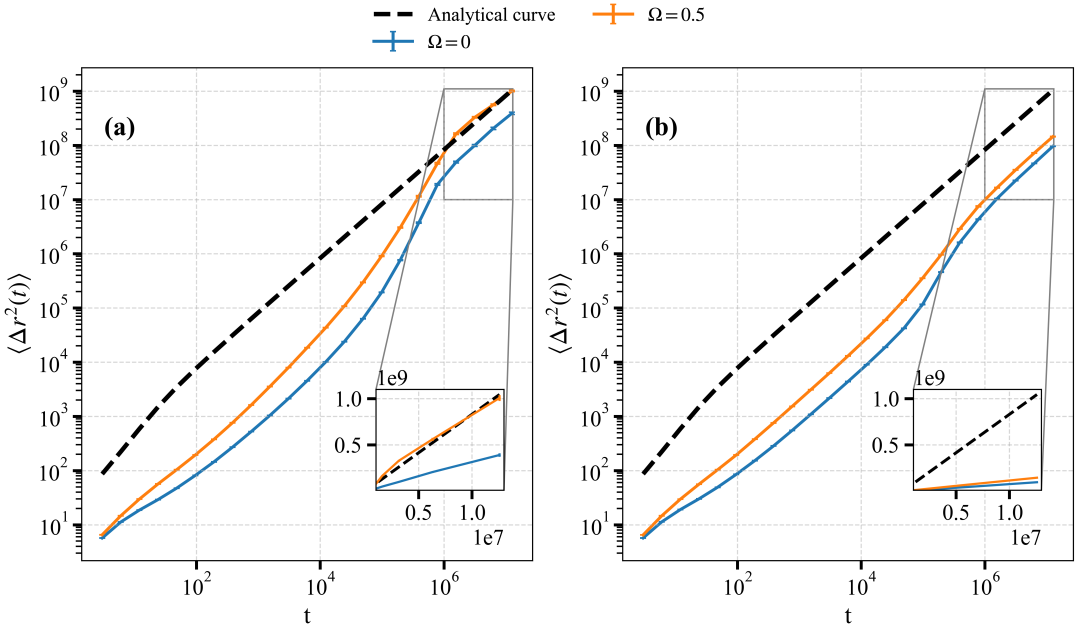

Figure 3.4: Mean Squared Displacement ($\langle \Delta \mathbf{r}^2(t) \rangle$). The black dashed line represents the analytical curve, indicating the expected free-diffusion behavior. The insets provide a zoomed-in view of the long-time regime in lin-lin scale, demonstrating the transition to a diffusive scaling. (a) $D_T = 0.0001$ and (b) $D_T = 0.001$.

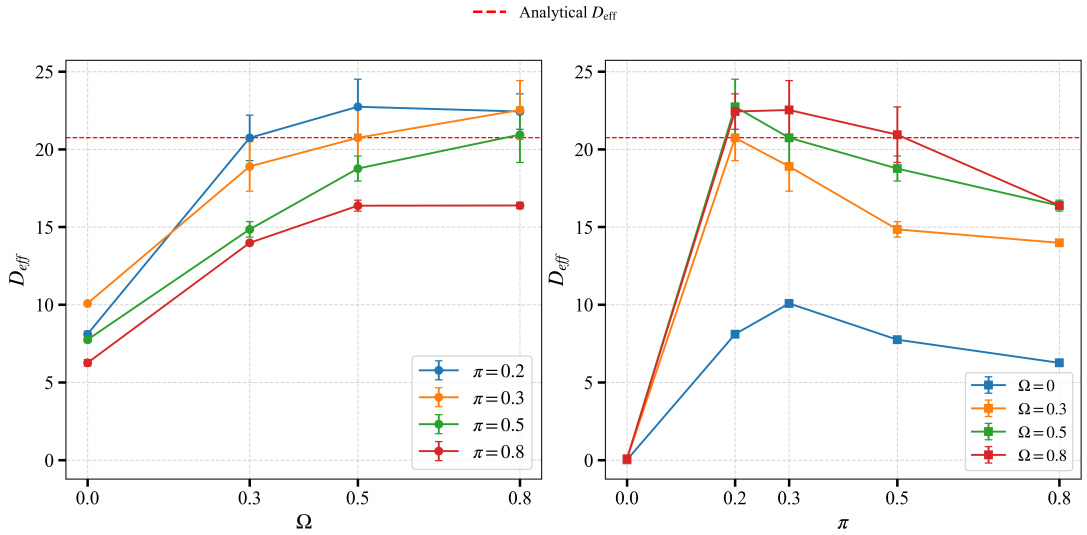

Figure 3.5: Effective diffusion coefficient (D_{eff}) as a function of (a) torque Ω, (b) push π for $D_T = 0.0001$. The red dashed line indicates the analytical value.

Panel (a) shows that D_{eff} increases monotonically with the realignment probability Ω. In this model, Ω does not represent a deterministic torque as in chiral active Brownian motion, but rather the stochastic probability that a particle realigns by $\pm 90^\circ$ when it cannot move forward (process b)). Larger Ω therefore facilitates more frequent escape from blocked configurations, reducing the time particles remain trapped and enhancing long-time transport. This effect is strongest for small translational diffusivity $D_T = 0.0001$, where motion is persistence-limited; at higher D_T, random thermal displacements already assist unjamming, so the dependence on Ω becomes weaker.

Panel (b) shows the effect of the push probability π, which instead leads to a non-monotonic dependence of D_{eff}. For small π, active particles are often immobilized because pushes are ineffective, while increasing π enhances the probability of successful displacement of passive obstacles, improving mobility. Beyond an optimal π, however, frequent pushing events promote local crowding and transient jamming of passive particles, which reduce overall transport efficiency. The interplay between π and Ω thus captures two complementary mechanisms — momentum transfer and realignment — that jointly determine the collective mobility of the active species [67, 68, 69, 70].

Varying the number of obstacles that can be pushed m changed only the time scale at which the results were obtained, so this analysis is not made in this chapter. Taken together, these results demonstrate that the interplay among rotational dynamics, translational noise, and environmental structure governs the emergent transport of active agents. The intermediate regime corresponds to transient path formation and local channeling, whereas the long-time diffusive limit reflects large-scale mixing and decorrelation of trajectories within the crowded matrix.

Chapter 4

Active-Passive Mixtures with Diffusivity Contrast

The phase separation observed in active-passive mixtures, where dense passive clusters form within a dilute active background, shares visual similarities with liquid-gas phase separation [71, 72, 73]. A fundamental question is whether this non-equilibrium demixing is accompanied by a true critical point, where the correlation length diverges and universal scaling laws are observed. While some studies suggest the presence of such criticality [71, 73, 74], it is not a universal feature of phase separation, and its existence and character can depend sensitively on microscopic details.

In particular, understanding how specific simulation parameters affect critical behavior requires systematic investigation of parameter spaces including activity levels (ϵ), rotation interaction (Ω) and system size (L). Previous studies indicate that microscopic dynamics — including activity, reorientation probability, and passive particle diffusion — can modify scaling exponents and alter the transition's nature [72, 75]. This chapter investigates whether a diffusivity contrast between active and passive particles can drive the system to a potential critical point and, if so, examines whether the associated scaling exponents exhibit universality or are sensitive to variations in the underlying dynamics.

Throughout this chapter, the term "diffusivity contrast" refers not to a spatial gradient, but exclusively to a difference in the effective thermal noise (diffusivity) between passive and active components, i.e., $D_T^{\text{passive}} \neq D_T^{\text{active}}$.

4.1 Active Particles in a Passive Bath

We investigate how differences in the effective temperature between active and passive species - implemented through distinct translational diffusion coefficients - affect phase separation in mixed systems. The simulation setup consists of systems with size $L = 40$, where we fix the active particle diffusivity at $D_T^{\text{active}} = 0.01$ and vary the passive particle diffusivity D_T^{passive} across the range 0.0007 to 0.01. Throughout this chapter, we use the notation $D_T \equiv D_T^{\text{passive}}$ for simplicity.

The simulations model binary mixtures with particle densities $\rho_p = 37.5\%$ for passive particles and $\rho_a = 1.1\%$ for active particles. Active particles have self-propulsion strength $\epsilon = 2$ and rotational diffusion coefficient $D_R = 0.123$, with push $\pi = 0.5$, $m = 1$. Each data point represents an average over 10^3 independent realizations. To ensure the system had fully equilibrated, measurements were sampled at $t = 10^6$, a point within the observed steady state.

We test two distinct rotation interaction regimes by comparing systems with zero torque ($\Omega = 0$) and non-zero torque ($\Omega = 0.5$). This comparison allows us to determine whether the observed phase separation behavior depends primarily on the relative mobilities of the components or is sensitive to the specific interaction dynamics.

To characterize the phase transition, we define two key observables evaluated at $t = 10^6$ during the steady-state regime. The first is the order parameter, ϕ, defined as the fraction of passive particles belonging to the largest cluster:

$$\phi = \frac{\text{size of largest passive cluster}}{N}, \tag{4.1}$$

where N is the total number of passive particles. This quantity captures the transition from a dispersed state ($\phi \approx 0$) to a macroscopically phase-separated one ($\phi \to 1$) [72, 76, 77, 74]. The second is the susceptibility, χ, which quantifies the fluctuations in the order parameter and typically peaks near phase transitions:

$$\chi = N\,\hat{\sigma}_\phi^2 = N \cdot \frac{1}{n-1}\sum_{i=1}^{n}(\phi_i - \bar{\phi})^2, \quad \text{with} \quad \bar{\phi} = \frac{1}{n}\sum_{i=1}^{n}\phi_i. \tag{4.2}$$

These are direct analogues to the order parameter and susceptibility in equilibrium phase transitions, making them appropriate for criticality analysis.

The peak in $\chi(D_T)$ helps identify the transition region, and we define the transition point D_c as the diffusion coefficient where the coexistence region terminates and the mixture becomes homogeneous in the large-system limit [71, 76].

To account for finite-size effects, we employ standard finite-size scaling relations. The susceptibility peak position $D_T^*(L)$ and peak height $\chi(D_T^*, L)$ scale with system size L as:

$$D_T^*(L) = D_c + CL^{-1/\nu}, \tag{4.3}$$

$$\chi(D_T^*, L) \sim L^{\gamma/\nu}, \tag{4.4}$$

where ν is the correlation-length exponent and γ is the susceptibility exponent. It is crucial to note that these scaling relations assume the system is sufficiently close to the true critical point and that finite-size effects dominate the scaling behavior. The exponents extracted from simulations using these relations are estimates for the thermodynamic limit, but may be affected by corrections-to-scaling and the limited system sizes accessible in simulations.

We now apply finite-size scaling analysis to systems with different rotation interactions, parameterized by the torque Ω. However, it is important to note that apparent power-law scaling in finite-size data

does not necessarily imply true criticality, as many non-critical crossovers can mimic such behavior over limited size ranges. The following analysis should therefore be interpreted as characterizing finite-size trends rather than definitively establishing universal critical exponents.

Table 4.1: Parameters and effective exponents extracted from finite-size scaling analysis.

Ω	ϵ	D_c	ν	γ/ν	γ
0	2	0.00230 ± 0.00004	0.52 ± 0.02	2.58 ± 0.08	1.35 ± 0.07
0.5	2	0.00356 ± 0.0007	1.2 ± 0.1	1.48 ± 0.08	1.75 ± 0.17

Figure 4.1 shows that both the peak position and peak height exhibit apparent power-law trends with system size. The physical significance of these effective exponents is as follows: the correlation-length exponent ν describes how the characteristic cluster size appears to diverge within our finite size range, while the ratio γ/ν quantifies how dramatically the order-parameter fluctuations grow with system size. The values for $\Omega = 0$ are markedly different from those for $\Omega = 0.5$, as is also visible in the distinct slopes shown in Fig. 4.1, suggesting that rotation interactions fundamentally alter the finite-size scaling behavior.

However, such power-law trends alone are insufficient to establish true criticality. The exponents extracted from peak fits represent effective scaling over the accessible system sizes and must be validated through full finite-size scaling collapse. We test for data collapse using the scaling form:

$$\chi(D_T, L)L^{-\gamma/\nu} = f\left[(D_T - D_c)L^{1/\nu}\right], \tag{4.5}$$

where $f(x)$ is a universal scaling function. A successful collapse would be consistent with a continuous phase transition, though deviations from perfect collapse may indicate systematic errors or that the system is not sufficiently close to criticality.

Given these apparent finite-size trends and their strong dependence on microscopic parameters, which already suggests non-universal behavior, we now rigorously test the consistency of the finite-size scaling hypothesis by examining the asymptotic behavior of the universal scaling function $f(x)$ from Eq. (4.5). In a standard continuous transition, the large-x limit of the scaling function should follow a power-law decay, $f(x) \sim x^{-\gamma}$, where the exponent γ is identical to the susceptibility exponent obtained from the peak-height scaling $\chi(D_T^*, L) \sim L^{\gamma/\nu}$. This provides a fundamental self-consistency check for the critical scaling ansatz.

Figure 4.2 shows the log-log finite-size scaling collapse for both torque values. While each individual curve for a fixed L exhibits an approximate power-law decay in the large-x regime, the rescaled susceptibility curves for different system sizes fail to collapse onto a single universal branch. The asymptotic tails remain vertically separated, indicating that the factor $L^{-\gamma/\nu}$ does not fully account for the system-size dependence. More decisively, the asymptotic slopes yield effective exponents:

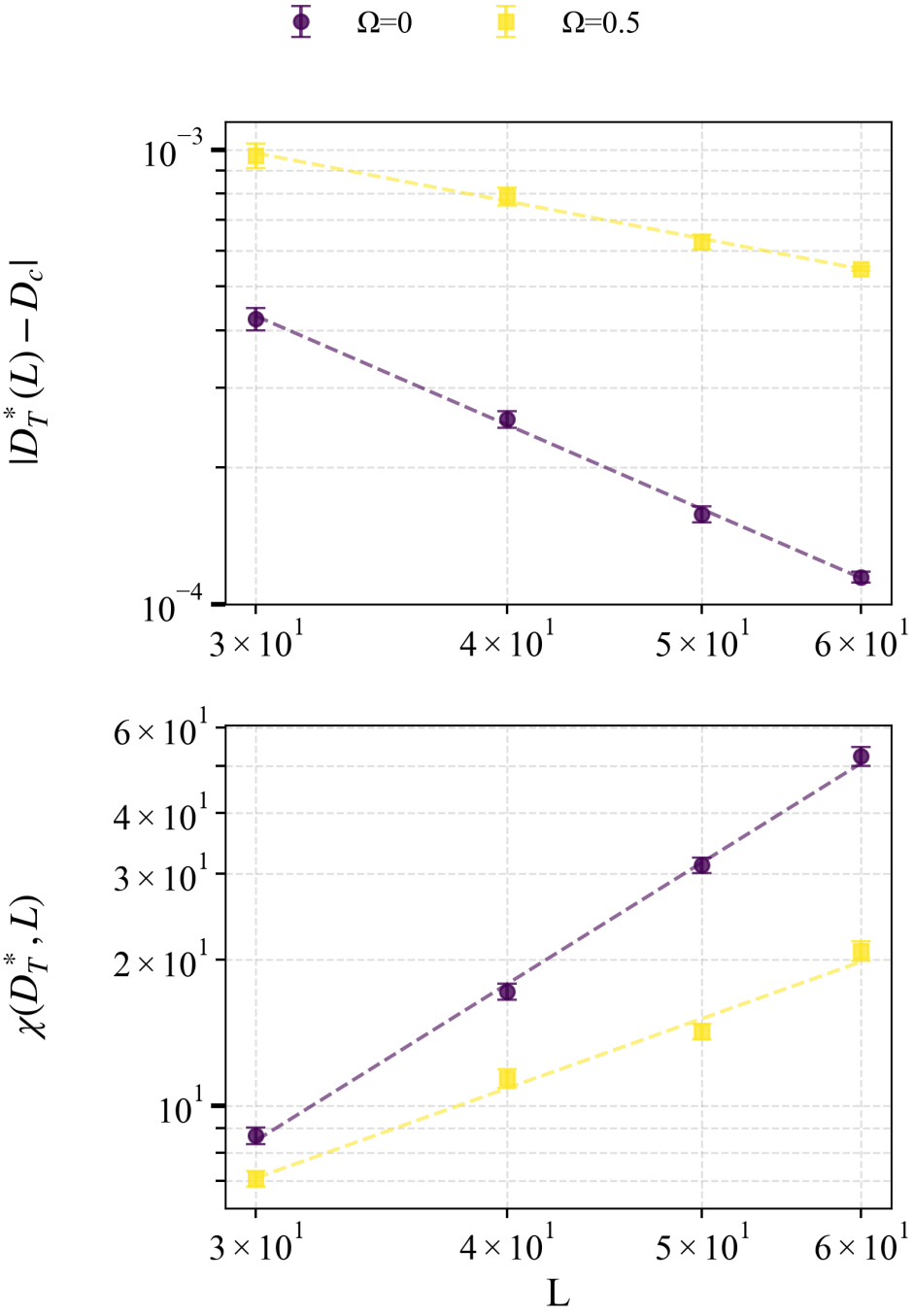

Figure 4.1: Finite-size scaling analysis for different Ω values, and activity $\epsilon = 2$. Data points were collected at $t = 10^6$ within the steady state. (Top) The shift of the susceptibility peak position $D_T^*(L) - D_c$ with system size $L^{-1/\nu}$. The dashed lines represent power-law fits used to extract the correlation-length exponent ν. (Bottom) The growth of the peak height $\chi(D_T^*, L)$ with system size. The dashed lines are fits to extract the exponent ratio γ/ν.

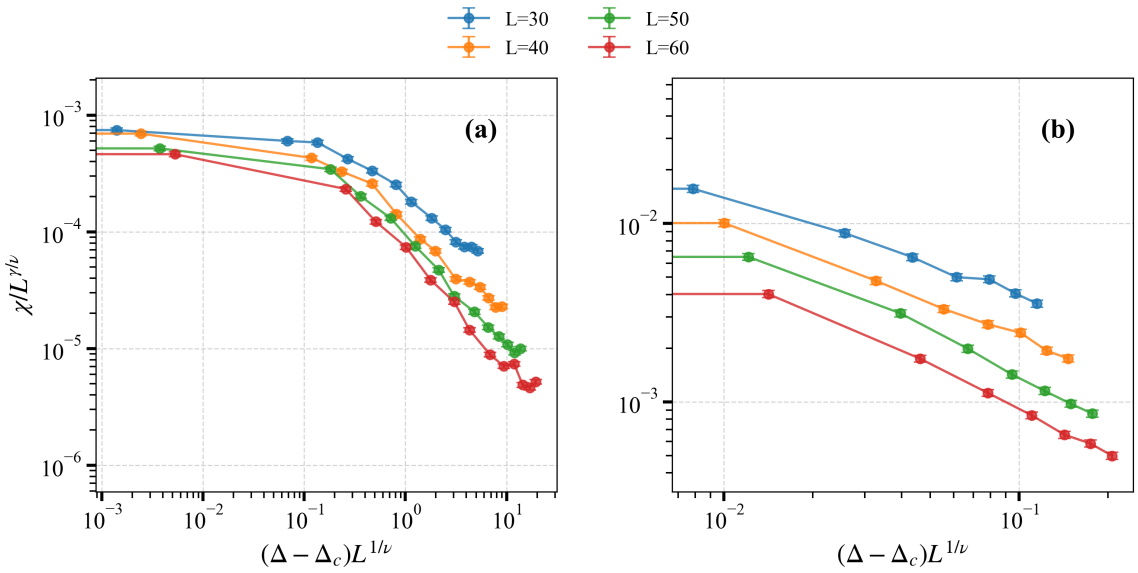

Figure 4.2: Log-log finite-size scaling test of the susceptibility for different system sizes L for (a) $\Omega = 0$ and (b) $\Omega = 0.5$, rescaled according to Eq. (4.5). Data are sampled at $t = 10^6$ within the steady-state regime.

- $\Omega = 0$: $\gamma \approx 0.90 \pm 0.04$
- $\Omega = 0.5$: $\gamma \approx 0.87 \pm 0.02$

These values are fundamentally incompatible with the respective exponents extracted from the peak-height scaling (Table 4.1).

This discrepancy violates the scaling hypothesis. The lack of a universal data collapse, combined with the inconsistent asymptotic exponents, demonstrates that the susceptibility defined via the largest passive cluster does not obey the finite-size scaling form of Eq. (4.5). Consequently, the apparent power-law scaling of the peak position $D_T^*(L)$ and height $\chi(D_T^*, L)$ with system size — while suggestive — cannot be interpreted as evidence of true criticality. Instead, it reflects a finite-size crossover behavior where the phase separation transition sharpens systematically with L, yet lacks the universal scaling properties characteristic of a continuous phase transition.

The failure of the scaling collapse suggests that the order parameter ϕ, based on the largest passive cluster, may not couple to a single diverging correlation length near the transition. In active matter systems, the interplay between phase separation and the non-equilibrium motility-induced instability can lead to rich, non-universal phenomenology. The effective exponents reported in Table 4.1 should therefore be understood as quantitative descriptors of how the transition sharpens with system size for this specific microscopic model and order parameter, rather than as universal critical exponents. This behavior is reminiscent of MIPS-like spinodal instabilities, where binodal and spinodal lines converge in the

large-system limit, producing a sharp but non-critical transition.

In summary, while a mobility contrast between active and passive components robustly tunes the location and finite-size sharpness of the demixing transition, our analysis reveals that it does not lead to a conventional critical point for the chosen order parameter. The observed scaling trends represent system-size dependent crossovers, and the extracted exponents are non-universal, varying significantly with microscopic parameters such as the torque Ω. This tunability and the breakdown of standard scaling underscore the rich, path-dependent behavior of phase transitions in active matter, which often elude classification into equilibrium universality classes.

Chapter 5

Tabletop experiment

Active systems provide a unique framework for exploring how local interactions and environmental structure give rise to emergent collective behaviors. While most studies focus on microscopic or simulated realizations, tabletop robotic models offer an accessible macroscopic platform for testing active-matter concepts under controlled and directly observable conditions. In this chapter, we investigate a system composed of Hexbugs — small, self-propelled robots powered by vibrational motors that act as analogues of active Brownian particles. Their persistent self-propulsion and stochastic reorientation capture the essential dynamics of active matter at a scale that enables direct measurement and visualization [78].

The main objective was to examine how the geometry of mobile obstacles affects collective motion and structure formation. Experimental observations are compared with computational simulations to identify robust behaviors and to determine how discretization of the environment influences emergent organization. The following sections describe the experimental setup, the influence of obstacle geometry on collective dynamics, and the connection between the tabletop system and the lattice-based model introduced earlier.

5.1 Experimental Setup and Measurement Design

This section details the experimental platform used to probe how obstacle geometry and mass influence collective transport. The system consists of Hexbug robots acting as self-propelled particles and 3D-printed obstacles serving as passive elements. At this macroscopic scale, parameters such as obstacle shape and inertia can be precisely controlled, providing a direct physical counterpart to the variables implemented in the lattice-based KMC model (Chapter 3). The design allows us to test whether the structures and dynamics predicted in simulations persist in a continuous, real-world environment.

Figure 5.1: HEXBUG robots used as macroscopic active particles, with approximate dimensions of $40 \times 15 \times 20$ mm and mass 7.2 g. Each device self-propels via internal vibration and undergoes random reorientation through frictional interactions.

The experimental system was designed to reproduce, in a controlled macroscopic setting, the essential ingredients of active-particle dynamics. The arena consisted of a custom-built wooden frame with smoothly curved boundaries that encouraged continuous motion and minimized trapping. The decision to use rounded boundaries was motivated by the well-established tendency of active particles to accumulate near rigid walls due to their persistent propulsion [42, 79, 80, 81, 82, 83]. This accumulation arises because particles continue to propel toward a surface until reorientation allows them to escape. Curved boundaries therefore reduce steady-state density gradients and ensure a more homogeneous exploration of the domain. A photograph of the full experimental arena is shown in Fig. 5.2.

HEXBUG robots acted as active agents, providing persistent propulsion and stochastic reorientation. Two obstacle geometries were employed — cubic and cylindrical — of comparable dimensions (2.5 cm of side and diameter, respectfully) but slightly different base mass. All obstacles were 3D printed as hollow structures open on one side, allowing the insertion of screws to adjust their mass. Table 5.1 summarizes the individual component masses.

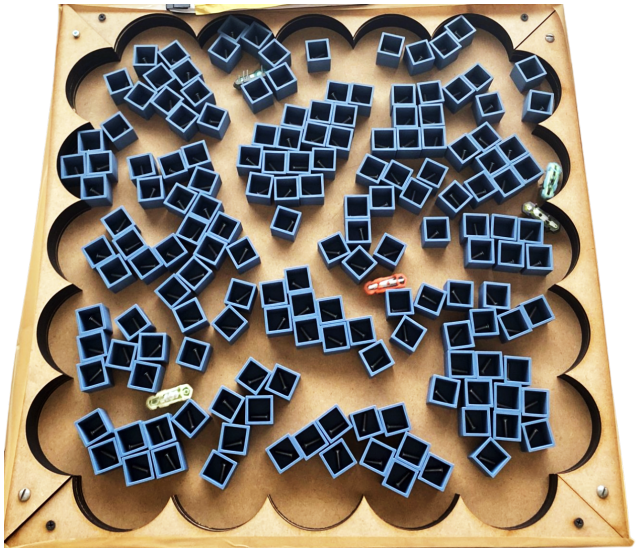

Figure 5.2: Top view of the experimental arena ($55.5 \times 55.5 \times 3.5$ cm) with curved boundaries with cubic obstacles and HEXBUG robots.

Table 5.1: Individual masses of the experimental components.

Component	**Mass (g)**
HEXBUG robots	7.2
Cubic obstacle (3D printed)	5.8
Cylindrical obstacle (3D printed)	5.1
Steel screw M5x16	2.8
Steel screw M5x20	4.1

Mobile obstacles were fabricated using 3D printing and manually distributed to achieve approximately uniform coverage of the arena floor before each run. Each experiment lasted fifteen minutes, corresponding to the stable operational time of the robots and allowing for steady-state configurations to develop. The configuration of obstacles (shape and number of inserted screws) was varied systematically across six trials to isolate the effects of geometry and mass on collective dynamics. Each trial included 162 mobile obstacles and 5 self-propelled robots.

System evolution was recorded from above using a fixed camera. Snapshots captured the motion of the robots and obstacles throughout each trial, documenting transient clustering, path formation, and large-scale rearrangements. In the present work, only qualitative visual inspection was performed to identify dominant structural patterns and interaction modes. However, the recorded image dataset provides a valuable basis for future quantitative analysis of trajectories, obstacle displacement, and collision

statistics.

To complement these qualitative observations of system evolution, we first quantify how the mass of individual obstacles affects robot transport efficiency. Understanding this single-obstacle dynamics provides a baseline for interpreting the collective rearrangements and emergent structures observed when many obstacles interact simultaneously. The next section presents controlled tunnel experiments designed to isolate and measure the effective velocity of robots pushing obstacles, which will later inform our analysis of collective behavior in the full arena.

5.2 Velocity Scaling and Comparison with Simulations

Measurements were performed in a narrow, quasi-one-dimensional tunnel (Figure 5.3) to quantify how obstacle mass affects transport efficiency. In this setup, a single robot pushed either a single obstacle whose mass was varied by adding one or more steel screws, or a chain of several light obstacles. In both cases, the effective obstacle mass was systematically increased, and the time required for the robot to push the load to the end of the tunnel (length $30\ \mathrm{cm}$) was recorded. The effective velocity was then obtained from the travelled distance divided by this measured time.

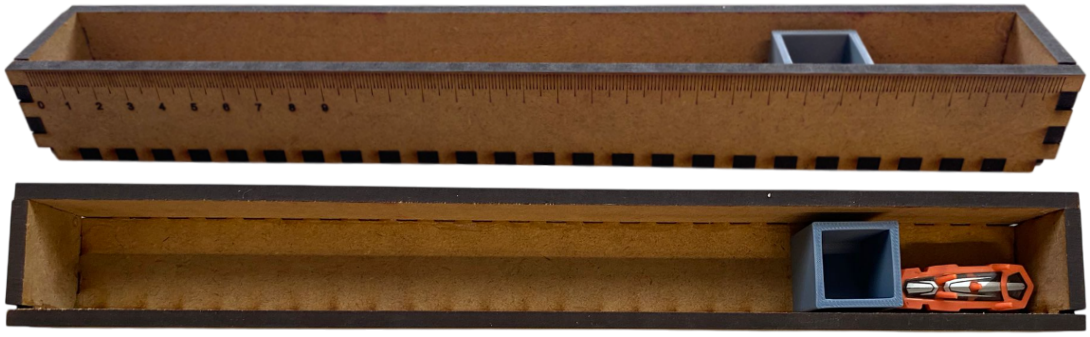

Figure 5.3: Custom-built tunnel used for controlled one-dimensional experiments to compare robot motion with 1D lattice simulations. The tunnel has a total length of $30\ \mathrm{cm}$. The outer walls include a laser-engraved ruler for precise position measurement.

This configuration isolates direct robot–obstacle interactions and allows an experimental analogy with the push probability parameter π from Chapter 3. In the computational model, π controls the probability that an active particle successfully displaces a passive one during a collision, effectively encoding the relative efficiency of momentum transfer.

The theoretical prediction for the velocity of an obstacle after a perfectly inelastic collision with a robot of initial velocity v_r follows from momentum conservation:

$$v_o = v_r \frac{m_r}{m_r + m_o}, \tag{5.1}$$

where m_r and m_o are the masses of the robot and obstacle(s), respectively. This idealized model neglects dissipation and assumes full momentum transfer in a single contact.

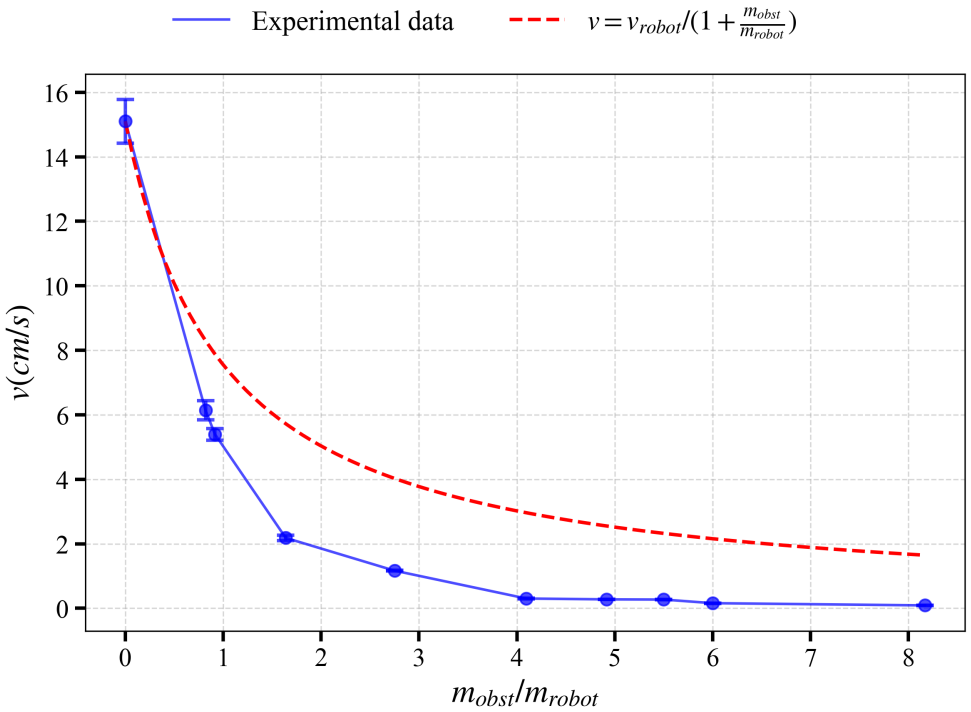

Figure 5.4: Measured obstacle velocity v_{eff} as a function of the mass ratio m_o/m_r. Blue circles denote experimental averages with standard-error bars, and the red dashed line corresponds to the ideal prediction from Eq. (5.1).

The steeper decay of the experimental data relative to the theoretical prediction indicates the presence of dissipation between robots and obstacles. Unlike the ideal inelastic impact model, momentum is transferred through multiple short interactions that involve frictional losses and vibrations. Small systematic deviations between successive measurements can also be attributed to gradual battery discharge during the sequence of trials, which slightly reduces the propulsion velocity of the robots over time.

In practice, these dissipative effects arise because robot–obstacle collisions deviate strongly from the idealized picture. The robot imparts momentum through repeated, short contacts that involve substantial energy loss by vibration, friction, and deformation. Consequently, the measured effective velocity decays more rapidly with increasing obstacle mass than predicted by Eq. (5.1). The dominant dissipative contribution scales approximately as $F_{\text{fric}} = \mu m_o g$, increasing linearly with mass and compounding inertial resistance. For heavier loads, robots spend longer recoiling and less time pushing, which reduces the mean effective velocity.

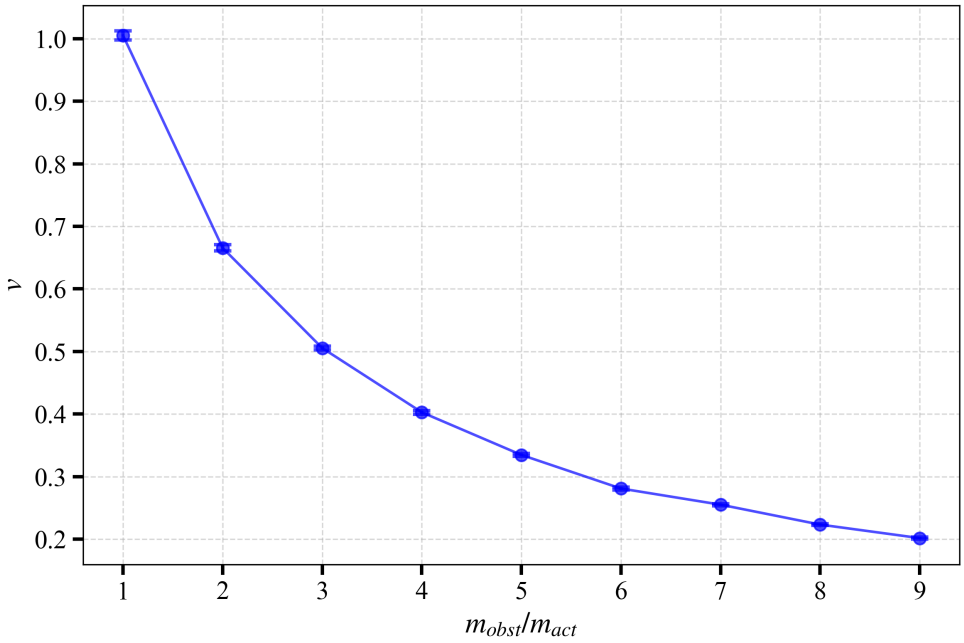

Figure 5.5: Simulation results: effective transport speed as a function of the mass ratio m_o/m_r introduced via the push probability π. Both experiment and simulation display a monotonic decay, supporting the identification of increased obstacle mass with decreased π.

The numerical results shown in Fig. 5.5 were obtained using the same KMC model described in Chapter 2, restricted here to a one-dimensional geometry to mirror the tunnel experiments. The system consists of a single active particle interacting with passive obstacles arranged along a line. The obstacle mass ratio m_o/m_r is incorporated in the model through the push probability π. For each value of π, simulation runs were performed and the effective transport velocity v_{eff} was calculated.

The agreement between the experimental and simulated velocity trends in Fig. 5.5 demonstrates that increasing obstacle mass plays the same role as decreasing the push probability π in the KMC model. Both parameters effectively reduce the rate of successful momentum transfer, leading to slower dynamics and decreased mobility. Despite the simplicity of the tabletop setup, the tunnel experiments capture the essential scaling behavior and reproduce the key features of active–passive coupling predicted by the theoretical framework.

Having established how obstacle mass influences single-robot transport efficiency, we now examine how obstacle geometry and mass combine to shape the collective structures that emerge in the multi-obstacle arena. These observations connect the velocity trends measured in the tunnel experiments with the formation of transient channels, clusters, and patterns in the full system.

5.3 Obstacle Geometry and Collective Structures

All the experiments described in this section had a duration of fifteen minutes. This time interval was chosen to ensure that steady-state configurations could develop while keeping the total duration of the experimental campaign manageable. Longer runs were avoided because the batteries of the HEXBUG robots have a maximum continuous operation of approximately $1.5\ \mathrm{h}$ of continuous operation, after which their propulsion speed decreases significantly. Each configuration was tested once, except for the cylindrical obstacles, which were repeated after the first trial due to a mechanical artifact: in the initial run, the robots entered through the open sides of the cylinders and became trapped. To prevent this, a transparent acrylic lid was subsequently placed on top of the arena in all later trials.

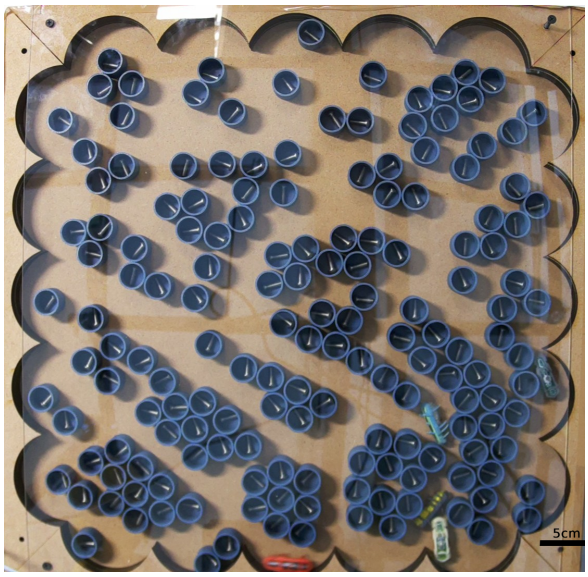

(a) Cylindrical obstacles with one screw: smooth trajectories and dynamic channels.

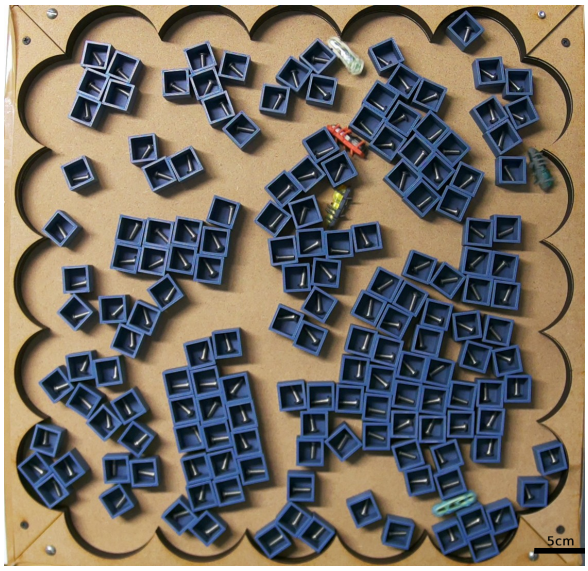

(b) Cubic obstacles with one screw: edge interlocking and rigid aggregates.

Figure 5.6: Effect of obstacle geometry at equal added weight. Cylindrical surfaces promote sliding interactions and fluid rearrangements, whereas cubic shapes enhance trapping, energy dissipation, and rigidity.

Obstacle geometry plays a dominant role in the emergent collective dynamics when the added weight per obstacle is identical (Fig. 5.6). As shown in Fig. 5.6(a), cylindrical obstacles facilitate sliding and rolling interactions, producing continuous trajectories and channels that reorganize dynamically. In contrast, cubic obstacles (Fig. 5.6(b)) promote interlocking along their edges, forming rigid aggregates that locally immobilize the robots. Collisions with cubes result in abrupt reorientations and longer contact times, enhancing dissipation and generating intermittent motion. Consequently, curved geometries support higher effective mobility and faster environmental rearrangement, whereas angular geometries favor

congestion and jamming.

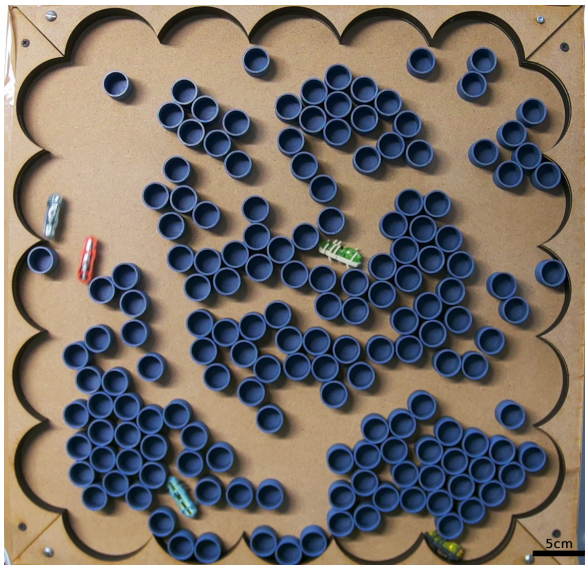

(a) Cylindrical obstacles without screws: highly mobile, rapidly rearranging configuration.

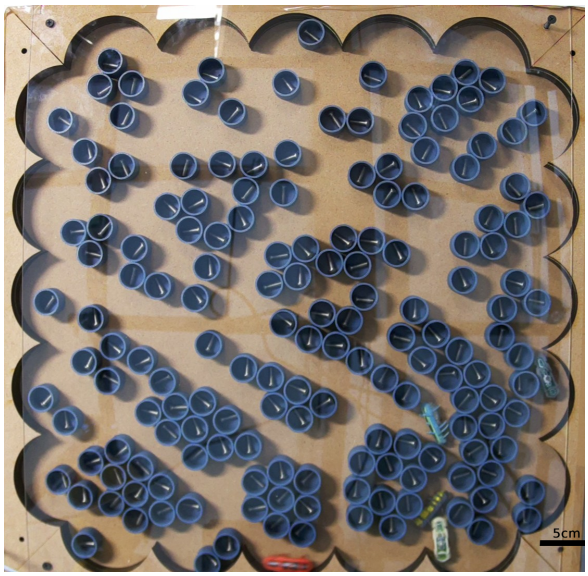

(b) Cylindrical obstacles with one screw: reduced rearrangement and increased local congestion.

Figure 5.7: Effect of obstacle mass for identical geometry (cylinders). Increasing mass reduces rearrangement and suppresses channel reorganization.

When geometry is kept fixed, increasing obstacle mass markedly alters the dynamics (Fig. 5.7). Lighter cylinders, without added screws (Fig. 5.7(a)), move readily upon collision, leading to frequent rearrangements and the formation of transport channels. Adding a screw to each cylinder increases mass and friction (Fig. 5.7(b)), resulting in longer contact times and more persistent blocked configurations. The overall mobility of both robots and obstacles decreases, consistent with the reduced pushing efficiency observed in the discrete model. For angular obstacles, added mass further stabilizes interlocked clusters and enhances rigidity, amplifying the onset of jamming.

Across all trials, no long-lived or permanent paths were observed, consistent with the stochastic reorganization characteristic of active systems. However, transient channels frequently appeared and were repeatedly reused before dissolving, reminiscent of the path formation phenomena described in Chapter 3.

A notable experimental artifact involves robot inversion events, which occurred frequently during experiments. When robots turn upside down, they remain mobile but exhibit markedly reduced propulsion and less controlled trajectories. This asymmetry introduces a state-dependent mobility: upright robots drive rearrangements and obstacle displacement, while inverted robots behave as quasi-passive elements that mostly undergo collisions or limited displacements. Frequent inversion thus contributes to the intermittent motion and localized congestion seen in Figs. 5.6–5.7. This effect is not represented in the discrete simulations, where all agents are assumed to maintain constant propulsion efficiency. This me-

chanical asymmetry represents an experimental limitation that could be mitigated by improving robot design or experimental setup to reduce flipping events, but it does not fundamentally alter the geometric and inertial trends identified in our study.

To explore the correspondence between experiment and theory, lattice-based simulations were performed using parameters chosen to qualitatively reproduce the experimental conditions. A representative snapshot is shown in Figure 5.8, where dense and dilute regions coexist in patterns qualitatively similar to those observed in the tabletop system.

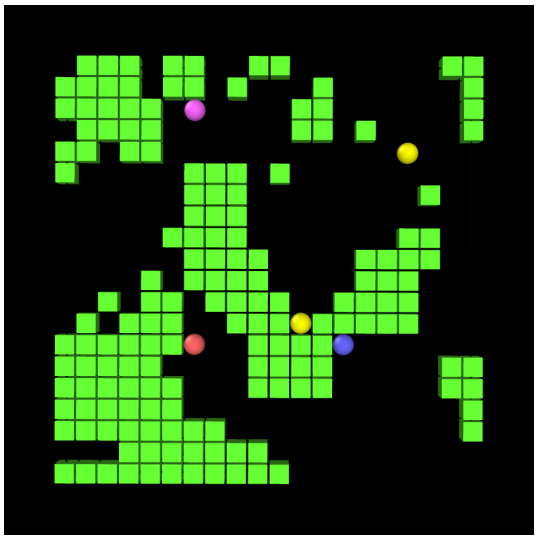

Figure 5.8: Simulation snapshot of the active–passive lattice system under parameters corresponding to the tabletop experiment. The clustering and transient pathways qualitatively reproduce experimental trends, confirming the influence of obstacle geometry on emergent structures. $t = 10^4$, $L = 20$,$\epsilon = 2$, $D_R = 0.123$, $D_T = 0.0001$, $\pi = 0.3$, $\Omega = 0.7$.

The qualitative agreement between experiment and simulation supports the interpretation that geometry and inertia together govern the transition between fluid-like and jammed states in active–passive systems.

While the main focus here is qualitative, the image dataset acquired during the experiments provides a solid basis for future quantitative studies. Subsequent analyses could quantify path formation through trajectory tracking, obstacle rearrangement via displacement measurements, cluster development using image segmentation techniques, and energy dissipation inferred from collision frequencies and robot displacement statistics. Such quantitative approaches would further strengthen the connection between macroscopic experiments and computational models of active–passive mixtures.

Chapter 6

Conclusion

Active matter systems provide a unique framework for studying the emergence of collective behaviors from simple local rules under non-equilibrium conditions. In such systems, interactions between active agents and their environment give rise to rich dynamics that depend strongly on crowding, confinement, and feedback mechanisms. This thesis aimed to investigate how environmental memory—arising from the capacity of active particles to reconfigure their surroundings—affects mobility, structure formation, and self-organization in heterogeneous environments.

Using a lattice-based Kinetic Monte Carlo (KMC) model, we developed a minimal yet versatile framework for active–passive coupling. The dynamics combine stochastic self-propulsion, translational diffusion, and rotational diffusion (with realignemnt probability Ω), together with excluded-volume interactions between active and passive particles. Within these excluded-volume rules, a pushing event occurs when an active particle encounters a finite chain of obstacles and displaces it forward with probability π (up to a cutoff m), thereby coupling particle motion to local environmental rearrangements and creating feedback. Systematically exploring this model over parameter space shows that Ω (rotational decorrelation) and π (momentum-transfer efficacy) act as complementary control knobs for mobility, clustering, and phase behavior in crowded media.

First, we verified that in the absence of passive particles, the model reproduces the characteristic features of Motility Induced Phase Separation (MIPS), a hallmark of active systems with purely repulsive interactions. The simulations revealed a clear transition from a homogeneous phase to coexistence between dense and dilute regions, with the emergence of a bimodal local density distribution consistent with previous theoretical and experimental studies.

Second, when mobile passive particles were introduced, the dynamics became dominated by the interplay between active propulsion and environmental restructuring. The system exhibited a transition from transient channel formation to large-scale phase separation. The analysis of local density distributions and passive-particle mobility demonstrated that crowding can drive organization through purely mechanical feedback, even in the absence of alignment or attraction. The push probability π and the realignment probability Ω were identified as control parameters governing this feedback. Intermediate values of π

maximize transport efficiency, while high values promote jamming and clustering. Increasing Ω reduces trapping by facilitating escape from blocked configurations, thus enhancing long-time diffusion. These results demonstrate that mobility in crowded active–passive mixtures emerges from the dynamic balance between persistence, reorientation, and environmental rearrangement.

Third, by decoupling the translational diffusivities of active and passive species, we investigated the influence of species-dependent motility on phase separation. Finite-size scaling analysis revealed that while the demixing transition sharpens systematically with system size, it does not exhibit universal scaling for the chosen order parameter. The apparent power-law trends and effective exponents were found to be non-universal, varying significantly with the torque. This demonstrates that the observed finite-size scaling reflects a non-critical crossover behavior rather than genuine criticality, underscoring how non-equilibrium phase separation can produce sharp but non-universal transitions that are highly sensitive to microscopic interaction rules.

Finally, to connect theory and experiment, a macroscopic analogue was developed using Hexbug robots as self-propelled agents and 3D-printed mobile obstacles as passive components. The experimental observations supported the simulation results: cubic obstacles promoted rigid clustering and energy dissipation, while cylindrical ones enabled smoother motion and continuous rearrangement. Measurements of effective velocity showed a faster decay with obstacle mass than predicted by ideal momentum conservation, confirming the role of dissipation and intermittent contact. The correspondence between increasing obstacle mass in experiments and decreasing push probability π in simulations validated the physical relevance of the model parameters.

Overall, this work establishes a unifying framework linking microscopic interaction rules to macroscopic transport and pattern formation in active–passive mixtures. The results highlight how self-organization in active matter arises not only from interactions among agents but also from the continual reshaping of the environment in which they move.

Beyond its relevance to the physics of active matter, this study provides insights into broader classes of systems where motion and environment are dynamically coupled. Examples include the collective migration of cells in complex tissues, the movement of microorganisms in porous or viscoelastic media, and the design of adaptive robotic swarms and responsive materials. The conceptual framework and modeling tools developed here thus contribute to the understanding and engineering of active systems across scales—from biological to synthetic.

The results presented in this thesis open several promising avenues for future research, both at the experimental and theoretical levels. Further developments can deepen the understanding of how environmental geometry, particle interactions, and feedback mechanisms govern collective behavior in active–passive mixtures.

From a modeling perspective, several extensions could enrich the theoretical framework developed here. A first direction would be to quantitatively characterize the anisotropy and curvature of spontaneously formed clusters, linking their morphology to underlying interaction parameters such as push probability and realignment dynamics. Measuring how these geometric descriptors evolve over time

could help identify characteristic coarsening scales and the lifetime of transient structures. Additionally, incorporating weak attractive interactions between active particles would allow testing how cohesion competes with motility-induced aggregation, establishing connections to biological collectives and synthetic active gels. Finally, the temporal evolution of particle trajectories could be analyzed through graph-based approaches to identify and characterize transient networks formed by particle motion, quantifying their connectivity, persistence, and structural evolution over time.

Within this modeling context, identifying an appropriate order parameter represents a crucial challenge, particularly one that properly captures the critical fluctuations in these non-equilibrium systems. The failure of the largest-cluster susceptibility to exhibit universal scaling suggests that multi-cluster statistics or a local density-based order parameter might be necessary to characterize the transition. Furthermore, systematically mapping the full parameter space—including activity ϵ, torque Ω, and density—could reveal whether genuine criticality exists for a different range of parameters or if the transition is inherently a non-critical crossover. Analytical work to derive effective hydrodynamic theories for these mixtures could also provide insight into the observed non-universal scaling.

It would also be valuable to establish a quantitative mapping between model parameters—such as the push probability π, the realignment probability Ω, and the translational diffusion D_T—and experimentally measurable quantities, including obstacle mass, surface friction, and robot velocity. This correspondence would enable systematic comparison between simulation and experiment, providing physical grounding to the parameter space explored computationally. In parallel, analytical treatments of the kinetic equations governing active–passive coupling could help identify universal scaling relations and link the discrete model to continuum or hydrodynamic descriptions.

On the experimental side, the tabletop robotic system can be refined to enable quantitative investigation of structure formation and transport dynamics. A particularly interesting direction would be to systematically vary the shape of mobile obstacles, starting from cubic geometries and progressively rounding their edges to form hexagonal, cylindrical, and eventually spherical shapes. Such a gradual modification would make it possible to study how curvature influences the transition between rigid, jammed configurations and fluid, reconfigurable assemblies. Parallel measurements of the characteristic lifetime and size of clusters would provide quantitative insight into the stability and evolution of emergent structures. Tracking these quantities across different obstacle shapes and masses could reveal scaling relations between inertia, aggregation, and orientational ordering, which preliminary observations suggest may lead to larger orientation domains at higher obstacle mass.

A complementary goal is to extract quantitative information from the video recordings acquired during the experiments. Automated image analysis could be employed to reconstruct trajectories, measure collision frequencies, and determine spatial correlation functions that characterize the degree of collective organization. Correlating the collision rate with obstacle mass would clarify how energy dissipation and friction control the effective dynamics of the system. Spatial mapping of collision events could also serve to identify regions of high mechanical activity, connecting dissipation to emergent path formation and collective transport. Although the present work focused on qualitative observations, such quantitative

analysis would provide a robust bridge between the macroscopic experiments and simulations.

Finally, the framework developed here could be generalized to include other forms of environmental feedback beyond mechanical displacement. Active particles that deposit or respond to chemical gradients, modify substrate stiffness, or reshape deformable boundaries would introduce additional coupling channels between motion and environment. Exploring these extensions would bring the model closer to real biological systems—such as migrating cells, bacteria navigating porous media, or self-organizing robotic collectives—and would open the way toward designing adaptive materials and autonomous active systems capable of exploiting environmental memory to coordinate their collective behavior.

Appendix A

Movement decision flowchart for process 1

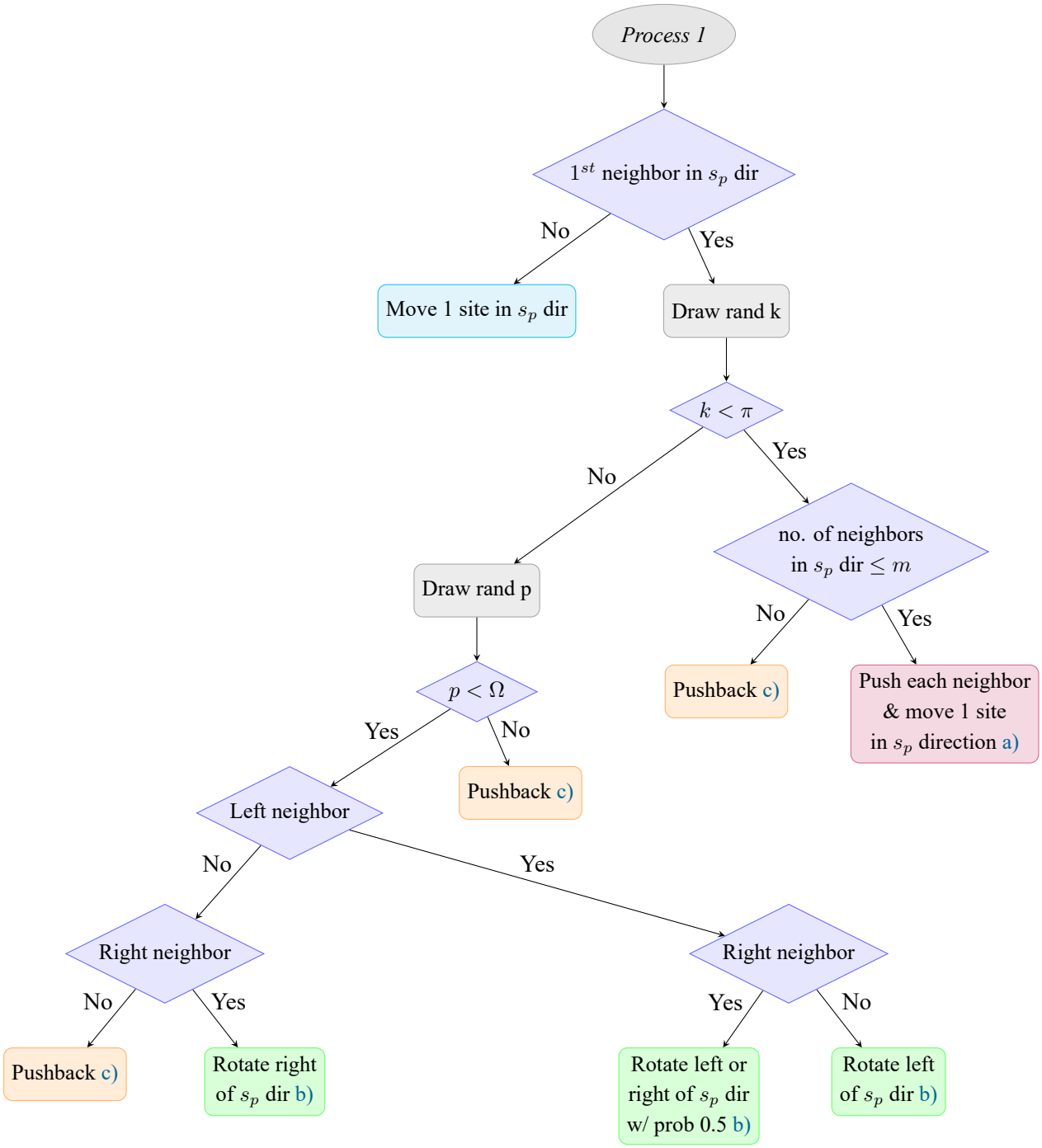
Process 1
1^{st} neighbor in s_p dir
No
Yes
Move 1 site in s_p dir
Draw rand k
$k < \pi$
No
Yes
Draw rand p
no. of neighbors in s_p dir $\leq m$
No
Yes
$p < \Omega$
Pushback c)
Push each neighbor & move 1 site in s_p direction a)
Yes
No
Pushback c)
Left neighbor
No
Yes
Right neighbor
Right neighbor
No
Yes
Yes
No
Pushback c)
Rotate right of s_p dir b)
Rotate left or right of s_p dir w/ prob 0.5 b)
Rotate left of s_p dir b)

Appendix B

1D Parameter mapping for D_{eff}

This appendix provides a detailed derivation of the effective diffusion coefficient D_{eff} for an active particle moving in one spatial dimension. The result supports the mapping relation for the geometric factor α presented in Section 2.3.3.

Analytically examining the one-dimensional case is particularly valuable because it provides an exact, tractable solution that captures the essential balance between self-propulsion, rotational decorrelation, and translational diffusion. This simplified geometry eliminates the complexities of higher-dimensional motion while preserving the physical mechanisms that determine long-time transport. The resulting expression for D_{eff} thus serves as a benchmark for validating numerical simulations and for generalizing the mapping to higher-dimensional systems.

We consider a single active particle moving on a 1D discrete lattice, with spacing Δx. The particle can move forward along its preferential direction with rate $\beta = \epsilon + \xi$, in the opposite direction with rate ξ, and switch its orientation at rate ω. The master equations governing the probability densities $P_+(x,t)$ and $P_-(x,t)$ (for right- and left-facing states, respectively) are

$$\begin{aligned}\frac{\partial P_\pm}{\partial t} &= \beta\left[P_\pm(x \mp \Delta x, t) - P_\pm(x,t)\right] \\ &\quad + \xi\left[P_\pm(x \pm \Delta x, t) - P_\pm(x,t)\right] \\ &\quad + \omega\left[P_\mp(x,t) - P_\pm(x,t)\right].\end{aligned} \tag{B.1}$$

Expanding $P_\pm(x \pm \Delta x, t)$ in a Taylor series and keeping terms up to second order gives a Fokker–Planck-like form,

$$\frac{\partial P_\pm}{\partial t} \approx \mp v\frac{\partial P_\pm}{\partial x} + D\frac{\partial^2 P_\pm}{\partial x^2} + \omega\left(P_\mp - P_\pm\right), \tag{B.2}$$

where the drift velocity and translational diffusion coefficient are defined as

$$v = (\beta - \xi)\Delta x, \qquad D = \frac{(\beta + \xi)\Delta x^2}{2}.$$

To solve these coupled equations, it is convenient to work in Fourier space. The Fourier transform of $P_{\pm}(x,t)$ is

$$\tilde{P}_{\pm}(k,t) = \int_{-\infty}^{\infty} P_{\pm}(x,t)\, e^{-ikx}\, dx, \tag{B.3}$$

which converts spatial derivatives into algebraic factors:

$$\mathcal{F}\left\{\frac{\partial P}{\partial x}\right\} = ik\tilde{P}, \qquad \mathcal{F}\left\{\frac{\partial^2 P}{\partial x^2}\right\} = -k^2\tilde{P}.$$

The transformed equations become

$$\frac{\partial \tilde{P}_+}{\partial t} = -ikv\,\tilde{P}_+ - k^2 D\,\tilde{P}_+ + \omega(\tilde{P}_- - \tilde{P}_+), \tag{B.4}$$

$$\frac{\partial \tilde{P}_-}{\partial t} = ikv\,\tilde{P}_- - k^2 D\,\tilde{P}_- + \omega(\tilde{P}_+ - \tilde{P}_-). \tag{B.5}$$

At $t = 0$ the particle is located at the origin and has equal probability of being oriented left or right,

$$P_{\pm}(x,0) = \frac{1}{2}\delta(x) \quad \Rightarrow \quad \tilde{P}_{\pm}(k,0) = \frac{1}{2}.$$

Next, we apply the Laplace transform in time,

$$\hat{P}_{\pm}(k,s) = \int_0^{\infty} e^{-st}\tilde{P}_{\pm}(k,t)\, dt,$$

which turns time derivatives into algebraic terms via $\mathcal{L}\left\{\partial_t \tilde{P}_{\pm}\right\} = s\hat{P}_{\pm} - \tilde{P}_{\pm}(k,0)$. The Laplace-transformed equations are then

$$(s + ivk + Dk^2 + \omega)\hat{P}_+ - \omega\hat{P}_- = \frac{1}{2}, \tag{B.6}$$

$$-\omega\hat{P}_+ + (s - ivk + Dk^2 + \omega)\hat{P}_- = \frac{1}{2}. \tag{B.7}$$

This linear system can be expressed compactly in matrix form:

$$\begin{bmatrix} s + ivk + A & -\omega \\ -\omega & s - ivk + A \end{bmatrix} \begin{bmatrix} \hat{P}_+ \\ \hat{P}_- \end{bmatrix} = \begin{bmatrix} 1/2 \\ 1/2 \end{bmatrix}, \quad \text{where } A = Dk^2 + \omega. \tag{B.8}$$

The determinant of the coefficient matrix is

$$\det(M) = (s + A)^2 + v^2k^2 - \omega^2,$$

and its inverse is

$$M^{-1} = \frac{1}{(s + A)^2 + v^2k^2 - \omega^2} \begin{bmatrix} s + A - ivk & \omega \\ \omega & s + A + ivk \end{bmatrix}.$$

Multiplying by the right-hand side yields

$$\hat{P}_+(k,s) = \frac{(s + A - ivk)/2 + \omega/2}{(s+A)^2 + v^2k^2 - \omega^2}, \tag{B.9}$$

$$\hat{P}_-(k,s) = \frac{(s + A + ivk)/2 + \omega/2}{(s+A)^2 + v^2k^2 - \omega^2}. \tag{B.10}$$

Summing over orientations gives the total probability density in Laplace–Fourier space:

$$\hat{P}(k,s) = \hat{P}_+ + \hat{P}_- = \frac{s + Dk^2 + 2\omega}{(s + Dk^2 + \omega)^2 + v^2k^2 - \omega^2}. \tag{B.11}$$

To obtain the time dependence, we invert the Laplace transform. Introducing $\lambda = \sqrt{\omega^2 - v^2k^2}$, we rewrite the denominator as

$$(s + Dk^2 + \omega)^2 - \lambda^2,$$

which allows decomposition into partial fractions,

$$\hat{P}(k,s) = \frac{A}{s + Dk^2 + \omega - \lambda} + \frac{B}{s + Dk^2 + \omega + \lambda},$$

with

$$A = \frac{\omega + \lambda}{2\lambda}, \qquad B = \frac{\lambda - \omega}{2\lambda}.$$

Performing the inverse Laplace transform gives

$$\tilde{P}(k,t) = Ae^{-(Dk^2+\omega-\lambda)t} + Be^{-(Dk^2+\omega+\lambda)t}.$$

For long times, the second exponential decays much faster ($\sim e^{-2\omega t}$), leaving

$$\tilde{P}(k,t) \approx \frac{\omega + \lambda}{2\lambda} e^{-(Dk^2+\omega-\lambda)t}.$$

In the limit of small wavenumbers ($kv/\omega \ll 1$), we expand λ as

$$\lambda = \sqrt{\omega^2 - v^2k^2} \approx \omega - \frac{v^2k^2}{2\omega},$$

so that

$$\tilde{P}(k,t) \approx e^{-(D+v^2/(2\omega))k^2 t}.$$

The term in parentheses defines the effective diffusion coefficient,

$$D_{\text{eff}} = D + \frac{v^2}{2\omega}.$$

Finally, performing the inverse Fourier transform yields the Gaussian propagator

$$P(x,t) = \frac{1}{2\pi}\int_{-\infty}^{\infty} e^{-D_{\text{eff}}k^2 t} e^{ikx} dk = \frac{1}{\sqrt{4\pi D_{\text{eff}} t}}\, e^{-x^2/(4D_{\text{eff}}t)}, \tag{B.12}$$

demonstrating that, at long times, the active particle behaves as an effective Brownian walker with

$$D_{\text{eff}} = (\xi + \beta)\frac{\Delta x^2}{2} + \frac{[(\beta - \xi)\Delta x]^2}{2\omega}.$$

This result confirms that at long times the active particle performs an effective diffusive motion with a renormalized diffusion coefficient incorporating both passive and active contributions. The first term, proportional to $(\xi + \beta)\Delta x^2/2$, represents the baseline translational diffusion arising from random hopping, while the second term, $v^2/(2\omega)$, captures the enhancement due to persistent self-propulsion over the characteristic reorientation timescale $1/\omega$. This decomposition provides the physical basis for the geometric mapping factor α introduced in Section 2.3.3, where analogous mechanisms govern the relationship between microscopic propulsion parameters and macroscopic transport in higher dimensions.

Appendix C

Parameter mapping for D_R

This appendix provides the detailed derivation of the rotational diffusion coefficient D_R for a particle on a lattice with angular discretization n, as summarized in Section 2.3.3.

The master equation for the probability $P(\theta, t)$ of a particle having orientation θ at time t, given discrete angular steps of size $\Delta\theta$ and turning probabilities q (left) and $p = 1 - q$ (right), is:

$$P(\theta, t + \Delta t) = q\, P(\theta - \Delta\theta, t) + (1 - q)\, P(\theta + \Delta\theta, t).$$

Expressing this in terms of rates $k_+ = (1 - q)/\Delta t$ and $k_- = q/\Delta t$, and noting that for our unbiased case $k_+ = k_- = \tau/2$ and $k = \tau$, the master equation can be rewritten as:

$$\frac{\partial P(\theta, t)}{\partial t} = k_-\, P(\theta - \Delta\theta, t) + k_+\, P(\theta + \Delta\theta, t) - kP(\theta, t). \tag{C.1}$$

We now derive a continuum approximation of this discrete master equation via Taylor expansion. Expanding the spatial terms $P(\theta \pm \Delta\theta, t)$ around θ gives:

$$P(\theta \pm \Delta\theta, t) \approx P(\theta, t) \pm \Delta\theta \frac{\partial P}{\partial \theta} + \frac{1}{2}\Delta\theta^2 \frac{\partial^2 P}{\partial \theta^2} + \mathcal{O}(\Delta\theta^3). \tag{C.2}$$

Substituting expansion (C.2) into the right-hand side of Equation (C.1) yields:

$$\begin{aligned} \frac{\partial P}{\partial t} \approx\ & k_- \left(P - \Delta\theta \frac{\partial P}{\partial \theta} + \frac{1}{2}\Delta\theta^2 \frac{\partial^2 P}{\partial \theta^2} \right) \\ & + k_+ \left(P + \Delta\theta \frac{\partial P}{\partial \theta} + \frac{1}{2}\Delta\theta^2 \frac{\partial^2 P}{\partial \theta^2} \right) - kP. \end{aligned}$$

Grouping similar terms:

$$\begin{aligned}\frac{\partial P}{\partial t} \approx\ & (k_- + k_+ - k)P \\ & + (-k_- + k_+)\Delta\theta \frac{\partial P}{\partial \theta} \\ & + \frac{1}{2}(k_- + k_+)\Delta\theta^2 \frac{\partial^2 P}{\partial \theta^2}.\end{aligned}$$

Since $k = k_+ + k_-$, the first term cancels to zero. Substituting $k_+ = k_- = \tau/2$ for the unbiased case simplifies the expression to:

$$\frac{\partial P}{\partial t} = \frac{1}{2}\tau\Delta\theta^2 \frac{\partial^2 P}{\partial \theta^2}. \tag{C.3}$$

This is the standard diffusion equation in angular space, $\frac{\partial P}{\partial t} = D_R \frac{\partial^2 P}{\partial \theta^2}$, from which we identify the rotational diffusion coefficient:

$$D_R = \frac{1}{2}\tau\Delta\theta^2. \tag{C.4}$$

Appendix D

Derivation of time increments in KMC

To derive the temporal increment Δt between events in a KMC algorithm, note that the waiting times separating consecutive events are distributed according to a Poisson process. This ensures that the probability of no events occurring over a given interval decays exponentially with the total rate of all possible transitions.

Figure D.1: Time interval $\Delta t + dt$ with infinitesimal increment dt.

Let $p(\Delta t)$ be the probability that no event has occurred in a time interval $[0, \Delta t]$. For an infinitesimal additional interval dt, the probability that an event occurs is $R_{\text{total}}\, dt$, where R_{total} is the sum of all event rates (Fig. D.1).

The probability of having no event by time $\Delta t + dt$ equals the probability of having no event by time Δt, minus the probability that an event occurs during the interval $[\Delta t, \Delta t + dt]$, that is,

$$p(\Delta t + dt) = p(\Delta t) - R_{\text{total}}\, dt\, p(\Delta t). \tag{D.1}$$

Dividing by dt and considering the limit $dt \to 0$, we obtain the differential equation:

$$\frac{p(\Delta t + dt) - p(\Delta t)}{dt} = -R_{\text{total}}\, p(\Delta t), \tag{D.2}$$

or, in standard differential form,

$$\frac{dp(\Delta t)}{dt} = -R_{\text{total}}\, p(\Delta t). \tag{D.3}$$

The minus sign reflects that the probability decreases with time, its rate of change set by both the present probability and the cumulative event rate. This is the standard equation for the decay of probability in a Poisson process, which underpins the stochastic timing in KMC.

Solving, we find the exponential distribution:

$$P(\Delta t) = e^{-R_{\text{total}}\Delta t}. \tag{D.4}$$

This solution gives the probability the system remains unchanged for at least time Δt. In simulations, it is necessary to draw random waiting times distributed according to this law. To do this efficiently, we employ the inverse cumulative method: a uniform random number $u \in (0, 1]$ is drawn, and we set

$$P(\Delta t) = u. \tag{D.5}$$

Solving for Δt,

$$\Delta t = -\frac{\ln u}{R_{\text{total}}}. \tag{D.6}$$

This formula produces waiting times that are correctly distributed, ensuring that the simulation clock advances in accordance with Poissonian statistics. By mirroring the stochastic nature of rare processes, this procedure guarantees that the elapsed time between transitions adheres to the true statistical distribution dictated by the rates, thereby faithfully reproducing the foundational physics of KMC algorithms.

References

[1] R. G. Loreto, A. G. Hart, T. M. Pereira, M. L. R. Freitas, D. P. Hughes, and S. L. Elliot, "Foraging ants trade off further for faster: use of natural bridges and trunk trail permanency in carpenter ants," *Naturwissenschaften*, vol. 100, no. 10, pp. 957–963, 2013. 1

[2] E. S. Gloag, L. Turnbull, and C. B. Whitchurch, "Bacterial stigmergy: An organising principle of multicellular collective behaviours of bacteria," *Scientifica*, vol. 2015, p. 387342, 2015. 1

[3] A. Boldini, M. Civitella, and M. Porfiri, "Stigmergy: from mathematical modelling to control," *Royal Society Open Science*, vol. 11, no. 9, p. 240845, 2024. 1

[4] C. S. Dias, M. Trivedi, G. Volpe, N. A. M. Araújo, and G. Volpe, "Environmental memory boosts group formation of clueless individuals," *Nat. Commun.*, vol. 14, p. 7324, 2023. 1, 6, 24

[5] P. W. Anderson, "More is different," *Science*, vol. 177, no. 4047, pp. 393–396, 1972. 1

[6] T. Vicsek, A. Czirók, E. Ben-Jacob, I. Cohen, and O. Shochet, "Novel type of phase transition in a system of self-driven particles," *Phys. Rev. Lett.*, vol. 75, no. 6, pp. 1226–1229, 1995. 1

[7] G. Ashkenasy, T. M. Hermans, S. Otto, and A. F. Taylor, "Systems chemistry," *Chem. Soc. Rev.*, vol. 46, pp. 2543–2554, 2017. 1

[8] W. Bialek, A. Cavagna, I. Giardina, T. Mora, E. Silvestri, M. Viale, and A. M. Walczak, "Statistical mechanics for natural flocks of birds," *Proceedings of the National Academy of Sciences*, vol. 109, no. 13, pp. 4786–4791, 2012. 1

[9] M. Granovetter, "Threshold models of collective behavior," *American Journal of Sociology*, vol. 83, no. 6, pp. 1420–1443, 1978. 1

[10] S. Ramaswamy, "The mechanics and statistics of active matter," *Annual Review of Condensed Matter Physics*, vol. 1, pp. 323–345, 7 2010. 1, 3

[11] M. E. Cates and J. Tailleur, "Motility-induced phase separation," *Annual Review of Condensed Matter Physics*, vol. 6, pp. 219–244, 2015. 1, 3, 18

[12] A. Bricard, J.-B. Caussin, D. Das, C. Savoie, V. Chikkadi, K. Shitara, O. Chepizhko, F. Peruani, D. Saintillan, and D. Bartolo, "Emergent vortices in populations of colloidal rollers," *Nature Communications*, vol. 6, p. 7470, 2015. 1

[13] R. G. Winkler and G. Gompper, "Hydrodynamics in motile active matter," in *Handbook of Materials Modeling*, pp. 1–21, Springer International Publishing, 2018. 1

[14] V. R. Misko, L. Baraban, D. Makarov, T. Huang, P. Gelin, I. Mateizel, K. Wouters, N. De Munck, F. Nori, and W. De Malsche, "Selecting active matter according to motility in an acoustofluidic setup: self-propelled particles and sperm cells," *Soft Matter*, vol. 19, pp. 8635–8648, 2023. 1

[15] B. A. Camley and W.-J. Rappel, "Physical models of collective cell motility: from cell to tissue," *Journal of Physics D: Applied Physics*, vol. 50, no. 11, p. 113002, 2017. 1

[16] R. Golestanian, T. B. Liverpool, and A. Ajdari, "Propulsion of a molecular machine by asymmetric distribution of reaction products," *Phys. Rev. Lett.*, vol. 94, p. 220801, 2005. 1

[17] J. R. Howse, R. A. L. Jones, A. J. Ryan, T. Gough, R. Vafabakhsh, and R. Golestanian, "Self-motile colloidal particles: From directed propulsion to random walk," *Phys. Rev. Lett.*, vol. 99, p. 048102, 2007. 1, 3, 4

[18] S. Sanchez, A. N. Ananth, V. M. Fomin, M. Viehrig, and O. G. Schmidt, "Superfast motion of catalytic microjet engines at physiological temperature," *Journal of the American Chemical Society*, vol. 133, pp. 14860–14863, 2011. 1

[19] R. Soto and R. Golestanian, "Self-assembly of catalytically active colloidal molecules: Tailoring activity through surface chemistry," *Phys. Rev. Lett.*, vol. 112, p. 068301, 2014. 1

[20] X. Ma, A. Jannasch, U.-R. Albrecht, K. Hahn, A. Miguel-López, E. Schäffer, and S. Sánchez, "Enzyme-powered hollow mesoporous janus nanomotors," *Nano Letters*, vol. 15, pp. 7043–7050, 2015. 1

[21] X. Ma, K. Hahn, and S. Sánchez, "Catalytic mesoporous janus nanomotors for active cargo delivery," *Journal of the American Chemical Society*, vol. 137, pp. 4976–4979, 2015. 1

[22] R. Dreyfus, J. Baudry, M. L. Roper, M. Fermigier, H. A. Stone, and J. Bibette, "Microscopic artificial swimmers," *Nature*, vol. 437, pp. 862–865, 2005. 1

[23] M. R. Shaebani, A. Wysocki, R. G. Winkler, G. Gompper, and H. Rieger, "Computational models for active matter," *Nature Reviews Physics*, vol. 2, pp. 181–199, 2020. 3, 6

[24] M. Sandoval and L. Dagdug, "Effective diffusion of confined active brownian swimmers," *Phys. Rev. E*, vol. 90, p. 062711, Dec 2014. 3

[25] O. Chepizhko and F. Peruani, "Diffusion, subdiffusion, and trapping of active particles in heterogeneous media," *Phys. Rev. Lett.*, vol. 111, p. 160604, 2013. 3

[26] C. Reichhardt and C. J. Olson Reichhardt, "Active matter transport and jamming on disordered landscapes," *Phys. Rev. E*, vol. 90, p. 012701, 2014. 3

[27] C. J. O. Reichhardt and C. Reichhardt, "Avalanche dynamics for active matter in heterogeneous media," *New Journal of Physics*, vol. 20, p. 025002, 2018. 3

[28] T. Jakuszeit, O. A. Croze, and S. Bell, "Diffusion of active particles in a complex environment: Role of surface scattering," *Phys. Rev. E*, vol. 99, p. 012610, 2019. 3

[29] A. Chamolly, T. Ishikawa, and E. Lauga, "Active particles in periodic lattices," *New Journal of Physics*, vol. 19, p. 115001, 2017. 3

[30] G. Volpe and G. Volpe, "The topography of the environment alters the optimal search strategy for active particles," *Proceedings of the National Academy of Sciences*, vol. 114, pp. 11350–11355, 2017. 3

[31] C. Yuan, A. Chen, B. Zhang, and N. Zhao, "Activity–crowding coupling effect on the diffusion dynamics of a self-propelled particle in polymer solutions," *Physical Chemistry Chemical Physics*, vol. 21, pp. 24112–24125, 2019. 3

[32] C. Kurzthaler, S. Mandal, T. Bhattacharjee, H. Löwen, S. S. Datta, and H. A. Stone, "A geometric criterion for the optimal spreading of active polymers in porous media," *Nature Communications*, vol. 12, p. 7088, 2021. 3

[33] J. Stenhammar, A. Tiribocchi, R. J. Allen, D. Marenduzzo, and M. E. Cates, "Continuum theory of phase separation kinetics for active brownian particles," *Phys. Rev. Lett.*, vol. 111, no. 14, p. 145702, 2013. 3

[34] R. Wittkowski, A. Tiribocchi, J. Stenhammar, R. J. Allen, D. Marenduzzo, and M. E. Cates, "Scalar ϕ^4 field theory for active-particle phase separation," *Nature Communications*, vol. 5, p. 4351, 2014. 3

[35] M. C. Marchetti, J.-F. Joanny, S. Ramaswamy, T. B. Liverpool, J. Prost, M. Rao, and R. A. Simha, "Hydrodynamics of soft active matter," *Rev. Mod. Phys.*, vol. 85, no. 3, pp. 1143–1189, 2013. 3, 5

[36] P. Romanczuk, M. Bär, W. Ebeling, B. Lindner, and L. Schimansky-Geier, "Active brownian particles," *The European Physical Journal Special Topics 2012 202:1*, vol. 202, pp. 1–162, 2012. 3, 17

[37] V. C. Braz, "Dynamics of active particles in the presence of obstacles," master's thesis, Faculdade de Ciências da Universidade de Lisboa, 2019. 4

[38] C. Bechinger, R. Di Leonardo, H. Löwen, C. Reichhardt, G. Volpe, and G. Volpe, "Active particles in complex and crowded environments," *Rev. Mod. Phys.*, vol. 88, p. 045006, 2016. 5

[39] T. Vicsek and A. Zafeiris, "Collective motion," *Physics Reports*, vol. 517, no. 3–4, pp. 71–140, 2012. 5

[40] A. Zöttl and H. Stark, "Emergent behavior in active colloids," *Journal of Physics: Condensed Matter*, vol. 28, no. 25, p. 253001, 2016. 5

[41] G. Gompper *et al.*, "The 2020 motile active matter roadmap," *Journal of Physics: Condensed Matter*, vol. 32, no. 19, p. 193001, 2020. 5

[42] K. J. Modica, Y. Xi, and S. C. Takatori, "Porous media microstructure determines the diffusion of active matter: Experiments and simulations," *Frontiers in Physics*, vol. 10, 4 2022. 5, 36

[43] R. Martinez, F. Alarcon, J. L. Aragones, and C. Valeriani, "Trapping flocking particles with asymmetric obstacles," *Soft Matter*, vol. 16, pp. 4739–4745, 2020. 5

[44] A. Martínez-Calvo, C. Trenado-Yuste, and S. S. Datta, "Active transport in complex environments," in *Out-of-equilibrium Soft Matter*, The Royal Society of Chemistry, 03 2023. 5

[45] R. Alonso-Matilla, B. Chakrabarti, and D. Saintillan, "Transport and dispersion of active particles in periodic porous media," *Phys. Rev. Fluids*, vol. 4, p. 043101, 4 2019. 5

[46] M. Mangeat, T. Guérin, and D. S. Dean, "Effective diffusivity of brownian particles in a two dimensional square lattice of hard disks," *The Journal of Chemical Physics*, vol. 152, p. 234109, 06 2020. 5

[47] M. J. Saxton, "Anomalous diffusion due to obstacles: a monte carlo study," *Biophysical Journal*, vol. 66, pp. 394–401, 2 1994. 5

[48] N. A. M. Araújo, L. M. C. Janssen, T. Barois, G. Boffetta, I. Cohen, A. Corbetta, O. Dauchot, M. Dijkstra, W. M. Durham, A. Dussutour, S. Garnier, H. Gelderblom, R. Golestanian, L. Isa, G. H. Koenderink, H. Löwen, R. Metzler, M. Polin, C. P. Royall, A. Šarić, A. Sengupta, C. Sykes, V. Trianni, I. Tuval, N. Vogel, J. M. Yeomans, I. Zuriguel, A. Marin, and G. Volpe, "Steering self-organisation through confinement," *Soft Matter*, vol. 19, pp. 1695–1704, 2023. 5

[49] A. Altshuler, O. L. Bonomo, N. Gorohovsky, S. Marchini, E. Rosen, O. Tal-Friedman, S. Reuveni, and Y. Roichman, "Environmental memory facilitates search with home returns," *Phys. Rev. Res.*, vol. 6, p. 023255, 2024. 6

[50] S. Makarchuk, V. C. Braz, N. A. M. Araújo, L. Ćirić, and G. Volpe, "Enhanced propagation of motile bacteria on surfaces due to forward scattering," *Nat. Commun.*, vol. 10, p. 4110, 2019. 6

[51] H. J. C. Berendsen, "Molecular dynamics simulations: The limits and beyond," in *Computational Molecular Dynamics: Challenges, Methods, Ideas* (P. Deuflhard, J. Hermans, B. Leimkuhler, A. E. Mark, S. Reich, and R. D. Skeel, eds.), (Berlin, Heidelberg), pp. 3–36, Springer Berlin Heidelberg, 1999. 6

[52] P. Español and B. Warren, P. "Perspective: Dissipative particle dynamics," *The Journal of Chemical Physics*, vol. 146, no. 15, p. 150901, 2017. 6

[53] B. Robertson, J. Schofield, P. Gaspard, and R. Kapral, "Molecular theory of langevin dynamics for active self-diffusiophoretic colloids," *The Journal of Chemical Physics*, vol. 153, no. 12, p. 124104, 2020. 6

[54] J. U. Klamser, O. Dauchot, and J. Tailleur, "Kinetic monte carlo algorithms for active matter systems," *Phys. Rev. Lett.*, vol. 127, p. 150602, Oct 2021. 7, 8

[55] M. Andersen, C. Panosetti, and K. Reuter, "A practical guide to surface kinetic monte carlo simulations," *Frontiers in Chemistry*, vol. 7, p. 202, 2019. 8

[56] K. A. Fichthorn and W. H. Weinberg, "Theoretical foundations of dynamical monte carlo simulations," *Journal of Chemical Physics*, vol. 95, no. 2, pp. 1090–1096, 1991. 8

[57] A. B. Bortz, M. H. Kalos, and J. L. Lebowitz, "A new algorithm for monte carlo simulation of ising spin systems," *Journal of Computational Physics*, vol. 17, no. 1, pp. 10–18, 1975. 8

[58] P. D. Neta, M. Tasinkevych, M. Telo da Gama, and C. S. Dias, "Wetting of a solid surface by active matter," *Soft Matter*, vol. 17, no. 9, p. 2468–2478, 2021. 8

[59] K. Reuter and M. Scheffler, "First-principles kinetic monte carlo simulations for heterogeneous catalysis: Application to the co oxidation at $\mathrm{Ruo_2}(110)$," *Phys. Rev. B*, vol. 73, p. 045433, Jan 2006. 8

[60] J. W. Evans, P. A. Thiel, and M. C. Bartelt, "Morphological evolution during epitaxial thin film growth: Formation of 2d islands and 3d mounds," *Surface Science Reports*, vol. 61, no. 1–2, pp. 1–128, 2006. 8

[61] M. J. Caturla, "Object kinetic monte carlo methods applied to modeling radiation effects in materials," *Computational Materials Science*, vol. 156, pp. 452–459, 2019. 8

[62] G. Gonnella, D. Marenduzzo, A. Suma, and A. Tiribocchi, "Motility-induced phase separation and coarsening in active matter," *Comptes Rendus Physique*, vol. 16, no. 3, pp. 316–331, 2015. Coarsening dynamics / Dynamique de coarsening. 18, 19

[63] H. Nakano and K. Adachi, "Universal properties of repulsive self-propelled particles and attractive driven particles," *Phys. Rev. Research*, vol. 6, p. 013074, 2024. 18

[64] J. Su, M. Feng, Y. Du, H. Jiang, and Z. Hou, "Motility-induced phase separation is reentrant," *Communications Physics*, vol. 6, p. 58, 2023. 18

[65] D. McDermott, C. Reichhardt, and C. J. O. Reichhardt, "Characterizing different motility-induced regimes in active matter with machine learning and noise," *Phys. Rev. E*, vol. 108, p. 064613, Dec 2023. 19

[66] J. Su, Z. Cao, J. Wang, H. Jiang, and Z. Hou, "Dynamical and thermodynamical origins of motility-induced phase separation," *Cell Reports Physical Science*, vol. 5, no. 2, p. 101817, 2024. 19

[67] S. van Teeffelen and H. Löwen, "Dynamics of a brownian circle swimmer," *Phys. Rev. E*, vol. 78, p. 020101, Aug 2008. 28

[68] B. ten Hagen, S. van Teeffelen, and H. Löwen, "Brownian motion of a self-propelled particle," *Journal of Physics: Condensed Matter*, vol. 23, p. 194119, apr 2011. 28

[69] M. Mijalkov and G. Volpe, "Sorting of chiral microswimmers," *Soft Matter*, vol. 9, no. 26, pp. 6376–6381, 2013. 28

[70] K. J. Modica, A. K. Omar, and S. C. Takatori, "Boundary design regulates the diffusion of active matter in heterogeneous environments," *Soft Matter*, vol. 19, pp. 1890–1899, 2023. 28

[71] J. Siebert, F. Dittrich, F. Schmid, K. Binder, T. Speck, and P. Virnau, "Critical behavior of active brownian particles," *Phys. Rev. E*, vol. 98, p. 030601, 2018. 29, 30

[72] F. Caballero and M. E. Cates, "Stealth entropy production in active field theories near ising critical points," *Phys. Rev. Lett.*, vol. 124, p. 240604, 2020. 29, 30

[73] B. Partridge and C. F. Lee, "Critical motility-induced phase separation belongs to the ising universality class," *Phys. Rev. Lett.*, vol. 123, no. 6, p. 068002, 2019. 29

[74] M. Sanoria, R. Chelakkot, and A. Nandi, "Percolation transition in phase-separating active fluid," *Phys. Rev. E*, vol. 106, p. 034605, 2022. 29, 30

[75] C. Maggi, M. Paoluzzi, A. Crisanti, E. Zaccarelli, and N. Gnan, "Universality class of the motility-induced critical point in large scale off-lattice simulations of active particles," *Soft Matter*, vol. 17, pp. 3807–3812, 2021. 29

[76] F. Fadda, D. A. Matoz-Fernandez, R. van Roij, and S. Jabbari-Farouji, "The interplay between chemo-phoretic interactions and crowding in active colloids," *Soft Matter*, vol. 19, pp. 2297–2310, 2023. 30

[77] F. Dittrich, T. Speck, and P. Virnau, "Critical behavior in active lattice models of motility-induced phase separation," *The European Physical Journal E*, vol. 44, p. 53, 2021. 30

[78] A. Barona Balda, A. Argun, A. Callegari, and G. Volpe, "Playing with active matter," *Am. J. Phys.*, vol. 92, pp. 847–858, 2024. 35

[79] G. Volpe, S. Gigan, and G. Volpe, "Simulation of the active brownian motion of a microswimmer," *American Journal of Physics*, vol. 82, pp. 659–664, 2014. 36

[80] A. Wysocki, J. Elgeti, and G. Gompper, "Giant adsorption of microswimmers: Duality of shape asymmetry and wall curvature," *Phys. Rev. E*, vol. 91, p. 050302, 2015. 36

[81] J. Elgeti and G. Gompper, "Wall accumulation of self-propelled spheres," *EPL (Europhysics Letters)*, vol. 101, p. 48003, 2013. 36

[82] A. P. Berke, L. Turner, H. C. Berg, and E. Lauga, "Hydrodynamic attraction of swimming microorganisms by surfaces," *Phys. Rev. Lett.*, vol. 101, p. 038102, 2008. 36

[83] T. Suphona, "Collective behaviors of autonomous robots in complex environment," master's thesis, Chalmers tekniska högskola, 2021. Submitted 2020. 36